Part III
Tower & Support Structure

Chapter 11
An Overview of Analysis and Design of Offshore Wind Turbines

Torgeir Moan and Tomasz Bugalski

Abstract Offshore wind provides an important source of renewable energy and new opportunities for marine technology. Various fixed and floating concepts have been proposed for offshore wind application. Offshore wind turbines (OWTs) with a monopile support structure fixed to the sea bed in shallow water, have already been industrialized, while fixed turbines in deeper water are emerging. Floating wind turbines are still at an early stage of development. The works presented in this chapter deal with selected recent developments of wind turbine concepts, design criteria and methods for integrated dynamic analysis. Besides design, topics such as inspection, monitoring, maintenance and repair during operation are also briefly addressed.

11.1 Introduction

An increased focus on renewable energy is needed in view of the climate challenges. Globally, there is a significant potential for offshore wind energy. Wind power is produced offshore by wind turbines that consist of a rotor, a drivetrain and an electric generator, supported on a tower and a bottom fixed or floating structure. The rotor can have a horizontal or vertical axis. While the horizontal axis turbines currently dominate the commercial market, vertical axis turbines provide advantages that especially could reduce the costs of floating turbines. The drivetrain is commonly a mechanical transmission with a gear but a hydraulic transmission or direct drive is also an alternative. For traditional wind turbines with gear transmissions, the gearbox is among the most expensive components.

T. Moan
Department of Marine Technology, Centre for Ships & Ocean Structures (CeSOS)/Centre for Autonomous Marine Operations & Systems (AMOS), Norwegian University of Science and Technology (NTNU), 7491 Trondheim, Norway
e-mail: torgeir.moan@ntnu.no

T. Bugalski (✉)
Centrum Techniki Okrętowej S.A. (Ship Design and Research Centre S.A), ul. Szczecińska 65, 80-392 Gdańsk, Poland
e-mail: tomasz.bugalski@cto.gda.pl

W. Ostachowicz et al. (eds.), *MARE-WINT*, DOI 10.1007/978-3-319-39095-6_11

Up until now, fixed foundations, such as monopile, gravity-base and tripod, are used in offshore wind farms in relatively shallow waters, i.e. 10–30 m depths. Jacket-type wind turbines have been installed in water depths up to 45 m and will play an important role in the near-future development. In deeper water, beyond 80 m, it may be more cost work effective to exploit wind resource by using floating wind turbines. This is because the foundation cost of a fixed wind turbine will increase significantly when the water depth increases, while the cost of a floater is less sensitive to the water depth.

The development of floating wind turbines is still at an early stage and further studies are required to demonstrate which of the concepts is the best one for certain site conditions, such as water depth and met ocean conditions. This not only requires due considerations of the support structure, but also of the rotor and drivetrain as wind turbines are tightly coupled systems where the different subsystems interact.

Fixed bottom wind turbines are usually designed as a de-coupled system. Hydrodynamic loads in deep water or intermediate water depth where wave profiles are not too steep, are well described by linear wave theory. As wave height increases and water depth decreases, the wave crest tends to become more narrow and steep, whereas the wave trough becomes long and flat. This happens as the wave starts to 'sense' the bottom. The nonlinearity of a wave increases with the wave steepness. Weakly non-linear undisturbed waves are in general well understood and for regular waves higher order perturbation solutions exist. Near the point of breaking, waves become highly nonlinear, and at the point of breaking release a high amount of energy; such events can have a significant impact on the loading on offshore wind turbines.

Spar-type floating wind turbines are suited for deep water due to their draft; Statoil plans to install five 6 MW spar turbines in 100 m water depth in Scotland.

So far semi-submersible wind turbines have been based on three columns connected by braces. Typically they are designed to support one central turbine or 1–3 turbines located on the top of columns. Clearly, if more than one turbines are installed on one platform, a weather-vaning mooring system will be needed to reduce the aerodynamic wake inter-action between them.

Alternative designs without braces have also been proposed. Current single 5 MW turbine concepts show a large scatter of displacement—between 4500 and 14,000 tons.

Tension-leg concepts normally require a displacement larger than a semi-submersible to ensure the necessary pretension of the tendons and hence the performance that implies limited heave, pitch and roll motions. The main challenge in tension-leg design is to satisfy the 'no slack' and limited maximum tension criteria for the tendons with a minimum displacement.

11.2 Research Activities in the MARE-WINT Project

Two types of large floating wind turbines are feasible for offshore applications—floating horizontal axis wind turbines (HAWTs) and floating vertical axis wind turbines (VAWTs). VAWTs have the potential to reduce the cost of energy, compared

to HAWTs. Chapter 12 thus deals with the integrated modeling and dynamic response analysis of typical floating VAWT concepts. A fully coupled aero-hydro-servo-elastic method is presented for numerical modeling and dynamic response analysis of floating wind turbine systems. In addition, comparative studies of floating HAWTs and VAWTs are performed.

Chapter 13 deals with hydrodynamic loads on a tripod substructure in relatively shallow water. It provides a brief review of existing analytical and empirical formulations and presents results of a numerical study, considering weak non-linear waves. Open-source codes were used in the simulation of breaking wave, with a focus on impulse forces.

The last chapter in this part (Chap. 14) deals with the use of condition monitoring (CM) and structural health monitoring (SHM) on the turbine tower. SHM allows early detection of damage and aids with maintenance planning, which reduces the cost. The SHM needs to be low cost, suitable for continuous measurement, insensitive to measurement noise, loading conditions and the ambient condition changes. While most efforts on CM and SHM of wind turbines are focused on the drivetrain, and to some extent on the blades, the purpose of this work has been to investigate the applicability of SHM for the tower.

In Chap. 14, a novel SHM technique, using the change in the location of the tower's Neutral Axis (NA) as a damage sensitive feature, is proposed. The method uses the Kalman Filter for the estimation of the NA location based on the measured strains along two mutually perpendicular axes. A decision based data fusion technique then allows the isolation of the damage. The use of NA as a damage sensitive feature allows the methodology to be insensitive to the ambient loading conditions, while the use of Kalman Filter allows temperature compensation and the robustness to the presence of measurement noise. The study has been carried out on the simulated finite element (FE) model of the wind turbine tower and indicates that bi-axial NA tracking based on data fusion is indeed necessary and at the same time is sensitive to damage. The proposed methodology is then validated using real strain data from the Nordtank NTK 500/41 wind turbine. Based on the results presented, it is concluded that a change in NA is indeed a robust damage indicator insensitive to ambient condition changes, and the applied loads.

Chapter 12
Dynamic Response Analysis of Floating Wind Turbines with Emphasis on Vertical Axis Rotors

Zhengshun Cheng, Torgeir Moan, and Zhen Gao

Abstract Large floating wind turbines are feasible for offshore application. Due to the commercial success onshore and nearshore, floating horizontal axis wind turbines (HAWTs) are now being widely studied. However, floating vertical axis wind turbines (VAWTs) have an excellent potential in the cost of energy reduction compared with floating HAWTs. This paper deals with the integrated modeling and dynamic response analysis of typical floating VAWT concepts. A fully coupled aero-hydro-servo-elastic method is presented for numerical modeling and dynamic response analysis of floating wind turbine systems. Considering a two-bladed 5 MW Darrieus rotor, the dynamic response characteristics of typical floating VAWT concepts are studied. In addition, comparative studies of floating HAWTs and VAWTs are performed.

12.1 Introduction

During the 1970s and 1980s, a large amount of efforts was devoted to develop VAWTs, particularly in the United States and Canada. However, the VAWTs gradually lost the competition with the horizontal axis wind turbines (HAWTs) due to low efficiency and fatigue problems within the bearings and blades. In recent years, offshore wind farms are moving towards deeper waters where floating wind turbines are required in countries such as the Japan, Norway and United States. Due to the commercial success onshore and nearshore, floating HAWTs are now being widely studied and prototypes have been developed and tested, such as the Hywind demo in Norway, the WindFloat demo in Portugal and the floating wind turbines off the Fukushima coast of northeast Japan.

The interest in the development of VAWTs for offshore application has also been resurging. Compared with floating HAWTs, floating VAWTs have lower centers of gravity, are independent of wind direction, can provide reduced machine complexity and have the potential of achieving more than 20 % cost of energy reductions

Z. Cheng (✉) • T. Moan • Z. Gao
Department of Marine Technology, Centre for Ships & Ocean Structures (CeSOS)/Centre for Autonomous Marine Operations & Systems (AMOS), Norwegian University of Science and Technology (NTNU), 7491 Trondheim, Norway
e-mail: zhengshun.cheng@ntnu.no; torgeir.moan@ntnu.no; zhen.gao@ntnu.no

W. Ostachowicz et al. (eds.), *MARE-WINT*, DOI 10.1007/978-3-319-39095-6_12

(Paquette and Barone 2012). Moreover, floating platforms can help to mitigate the fatigue damage suffered by the onshore VAWTs (Wang et al. 2016). In addition, floating VAWTs are more suitable for deploying as wind farms than floating HAWTs (Dabiri 2011). Thus, more and more efforts are devoted to the development of floating VAWTs.

In order to assess the technical feasibility of floating VAWTs, a numerical simulation tool is required to conduct the fully coupled aero-hydro-servo-elastic analysis. To date the available simulation tools that can model the floating VAWTs in a fully-coupled way are limited, but are emerging, such as the FloVAWT code by Cranfield University (Collu et al. 2013), the OWENS toolkit by Sandia National Laboratories (Brian et al. 2013), the HAWC2 by DTU Wind Energy (Larsen and Madsen 2013), the SIMO-RIFLEX-DMS (Wang et al. 2013) and SIMO-RIFLEX-AC (Cheng et al. 2016b) code by NTNU. Among these codes, the aerodynamic loads are mainly computed using the double multi-streamtube (DMS) model (Paraschivoiu 2002) or actuator cylinder (AC) flow model (Madsen 1982), which are capable of predicting the aerodynamic loads accurate at a small computational cost. These two models are validated using experimental data by Wang et al. (2015b) and Cheng et al. (2016a). Code-to-code comparisons between these codes were also conducted to verify each code, such as the comparison of FloVAWT and SIMO-RIFLEX-DMS by Borg et al. (2014c), and the comparison of three codes SIMO-RIFLEX-DMS, SIMO-RIFLEX-AC and HAWC2 by Cheng et al. (2016b).

Considerable efforts have been made to study the floating VAWTs by many researchers using the aforementioned codes. Using the code HAWC2, Paulsen et al. (2013) performed a design optimization of the proposed DeepWind concept. An improved design has been obtained with an optimized blade profile with less weight and higher stiffness than the 1st baseline design. Based on the code FloVAWT, Borg et al. (2014a, b) presented a review on the dynamic modeling of floating VAWTs, used a wave energy converter as a motion suppression device for floating wind turbines (Borg et al. 2013) and further performed a comparison on the dynamics of floating VAWTs with three different floating support structures (Borg and Collu 2014). A floating VAWT concept with a 5 MW Darrieus rotor mounted on a semi-submersible was proposed by Wang et al. (2013) and fully coupled aero-hydro-servo-elastic simulations were carried out with emphasis on stochastic dynamic responses (Wang et al. 2016), effects of second order difference-frequency forces and wind-wave misalignment (Wang et al. 2015a), and emergency shutdown process with consideration of faults (Wang et al. 2014a).

In this study, dynamic response characteristics of typical floating VAWTs are addressed. The development and verification of fully coupled numerical simulation tools SIMO-RIFLEX-DMS and SIMO-RIFLEX-AC are presented. Using a two-bladed 5 MW Darrieus rotor, dynamic responses of three floating VAWT concepts (Cheng et al. 2015a, 2015c) are studied by fully coupled nonlinear time domain simulations. In addition, comparative studies of the dynamic responses of floating HAWTs with the NREL 5 MW wind turbine (Jonkman et al. 2009) and VAWTs with the 5 MW Darrieus rotor (Vita 2011) are also performed to assess the merits and disadvantages of each concept.

12.2 Typical Floating VAWT Concepts

Currently several floating VAWT concepts have been proposed, including the DeepWind (Vita 2011), VertiWind (Cahay et al. 2011) and floating tilted axis (Akimoto et al. 2011) concepts. They are comprised of a vertical axis rotor, a floater and a mooring system. The rotor can be straight-bladed H-type rotor, curve-bladed Darrieus rotor, helical-bladed rotor and V-type rotor, while the floater could be a spar, semi-submersible or TLP.

Herein three floating support structures were studied: namely a spar, a semi-submersible and a TLP, as depicted in Fig. 12.1 and listed in Table 12.2. The concepts were used to support a 5 MW Darrieus rotor, which is the baseline design developed in the DeepWind project (Vita 2011). The rotor is comprised of two blades and one rotating tower that spans from the top to the bottom that is connected to the generator. Main specifications of this rotor are summarized in Table 12.1. The generator considered here was assumed to be placed at the tower base, and the generator mass was incorporated in the platform hull mass.

The concepts were originally designed to support the NREL 5 MW wind turbine (Jonkman et al. 2009). The concepts were considered in the water depth where they were designed, ranging from 150 m for the TLP, 200 m for the semi to 320 m for the spar. Here reasonable modifications were made on each platform to support the 5 MW Darrieus rotor, such as adjusting the ballast of the spar and the semi, and the tendon pretension of the TLP. For each platform, the draft and displacement were maintained the same as the original one. Details regarding the adjustment can refer to Cheng et al. (2015c). Properties related to the three floating VAWT systems are given in Table 12.2. The natural periods of rigid body motions for the floating

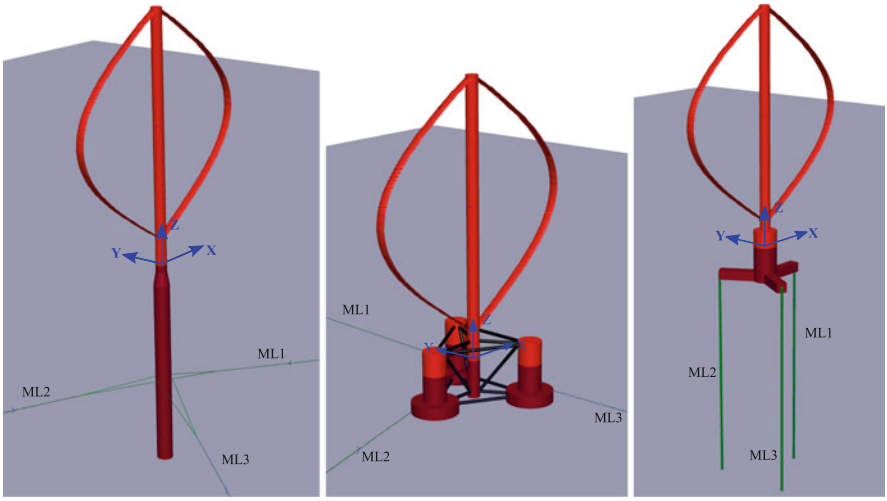

Fig. 12.1 Three floating VAWT concepts: spar, semi-submersible and TLP

Table 12.1 Specifications of the Darrieus 5 MW wind turbine

	Darrieus rotor
Rated power [MW]	5
Rotor radius [m]	63.74
Rotor height, root-to-root [m]	129.56
Chord length [m]	7.45
Cut-in, rated, cut-out wind speed [m/s]	5, 14, 25
Rated rotor rotational speed [rpm]	5.26
Total mass, including rotor, shaft and tower [kg]	754,226
Location of overall center of mass [m]	(0, 0, 75.6)

Table 12.2 Properties of the three floating wind turbine systems

Floater	Spar	Semi-submersible	TLP
Water depth [m]	320	200	150
Draft [m]	120	20	22
Diameter at mean water line [m]	6.5	12.0/6.5	14.0
Platform mass, including ballast & generator [ton]	7308.3	13353.7	2771.9
Center of mass for platform [m]	(0, 0, −89.76)	(0, 0, −15.38)	(0, 0, −13.42)
Buoyancy in undisplaced position [kN]	80,710	139,816	56,804
Center of buoyancy [m]	(0, 0, −62.07)	(0, 0, −13.15)	(0, 0, −14.20)
Surge/Sway natural period [s]	130.8	114.0	45.3
Heave natural period [s]	27.3	17.1	0.6
Roll/Pitch natural period [s]	34.5	31.0	4.5/4.9
Yaw natural period [s]	8.5	79.7	19.3

systems were estimated by conducting free decay tests using numerical simulations (Cheng et al. 2015c).

Since the difference in mass between the 5 MW Darrieus rotor and the NREL 5 MW wind turbine was small compared to the displacements of these three concepts, it was assumed that such modifications would not alter the hydrostatic performance of each platform significantly, which was verified by the following simulations. After these modifications, these substructures supporting the 5 MW Darrieus rotor may not be optimal from an economical point of view, but they are sufficient to demonstrate the inherent motion and structural response characteristics of each concept.

12.3 Integrated Modeling of a Floating VAWT System

A floating wind turbine system is usually comprised of a rotor harvesting wind energy, a floater supporting the rotor and a mooring system keeping the floater in position. To evaluate its performance, a fully coupled aero-hydro-servo-elastic

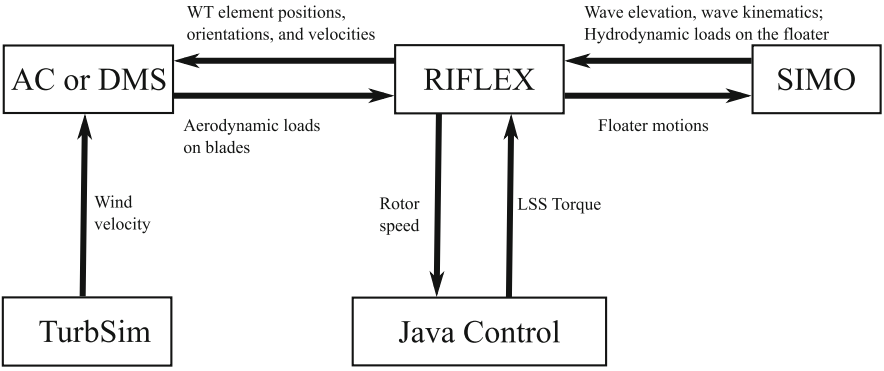

Fig. 12.2 Overview of the fully coupled aero-hydro-servo-elastic codes SIMO-RIFLEX-DMS and SIMO-RIFLEX-AC

simulation tool is required to carry out the time domain simulations similar as those used for analysis of floating HAWTs. This coupled code should account for the aerodynamics, hydrodynamics, structural dynamics, controller dynamics and mooring line dynamics. Currently, two fully coupled codes, namely SIMO-RIFLEX-DMS and SIMO-RIFLEX-AC, are developed in NTNU to conduct such fully integrated modeling and analysis for floating VAWTs. These two codes are based on the codes SIMO (MARINTEK 2012b) and RIFLEX (MARINTEK 2012a), which are originally developed and are now widely used in the offshore oil & gas industry. The SIMO-RIFLEX wind turbine module has previously been verified (Luxcey et al. 2011; Ormberg et al. 2011).

As illustrated in Fig. 12.2, each coupled code integrates three computer codes, including the SIMO (MARINTEK 2012b), RIFLEX (MARINTEK 2012a) and an aerodynamic module. SIMO computes the hydrodynamic forces and moments on the floater; RIFLEX represents the blades, tower, shaft and mooring lines as non-linear flexible finite elements and provides the links to an external controller and an aerodynamic module. Obviously, the significant difference between these two codes lies in the method used to compute the aerodynamic loads. Detailed discussions about the related aerodynamic theories are demonstrated in Sect. 12.3.1. In addition, the external controller based on two different control strategies is written in Java. In this way, each of these two fully coupled codes can provide a comprehensive aero-hydro-servo-elastic simulation tool with well-known aerodynamic module, sophisticated hydrodynamic model, stable nonlinear finite element solver, and user-defined controller.

In each fully coupled code, the blades, shaft, tower and mooring lines are modeled as nonlinear flexible finite elements while the floater is considered as a rigid body. Detailed structural model for each component and the corresponding external load models are illustrated in Fig. 12.3. The aerodynamic force is computed in the aerodynamic module as distributed lift and drag forces along the blade and then transferred from the rotor to the generator. The first- and second-order

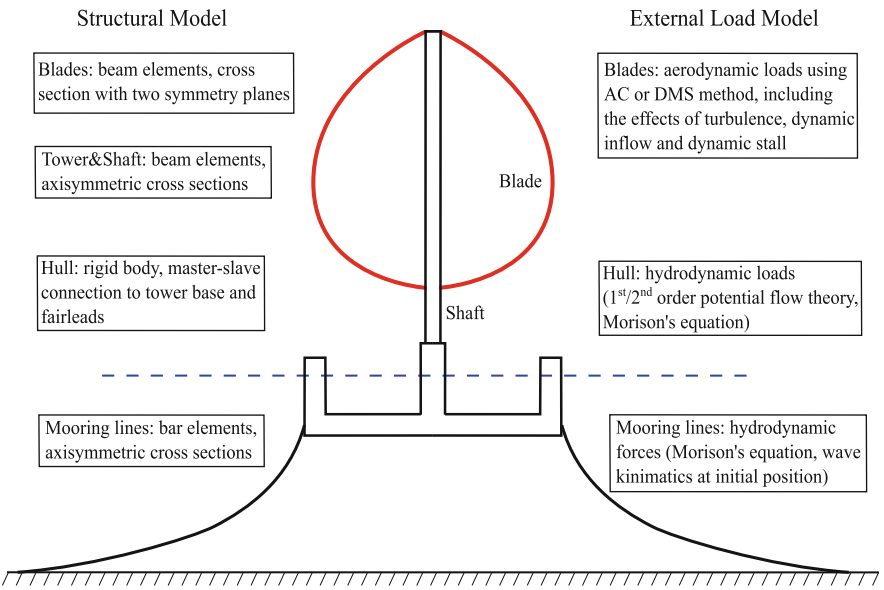

Fig. 12.3 The structural model and external force model of a floating VAWT (Cheng et al. 2016b)

wave excitation forces on the floater are pre-generated in SIMO, while the viscous drag forces on the floater are updated. At each time step, the dynamic equilibrium equations of the rotor, platform and mooring lines are solved in RIFLEX and the rotor rotational speed is regulated through the external controller. Then the platform motions are transferred to SIMO to update the viscous drag forces on the floater, while the positions, velocities and accelerations of the blade elements are transferred to the aerodynamic module to update the aerodynamic loads.

12.3.1 Aerodynamics

Among the aerodynamic models for VAWTs, the Double Multiple-Streamtube (DMS) model (Paraschivoiu 2002) and Actuator Cylinder (AC) flow method (Madsen 1982) are two favorable methods that are suitable for fully coupled modeling and analysis for floating VAWTs. Based on these two methods, two aerodynamic codes are developed for fully coupled modeling and analysis of floating VAWTs by Wang et al. (2015b) and Cheng et al. (2016a), respectively.

The DMS method is based on the conservation of mass and momentum in a quasi-steady flow. It assumes that the rotor is vertically divided into a series of adjacent streamtubes, within which a pair of actuator disks are used to represent the turbine. Then the forces on the rotor blades are equated to the change in the streamwise momentum through the turbine, so as to calculate the axial induction

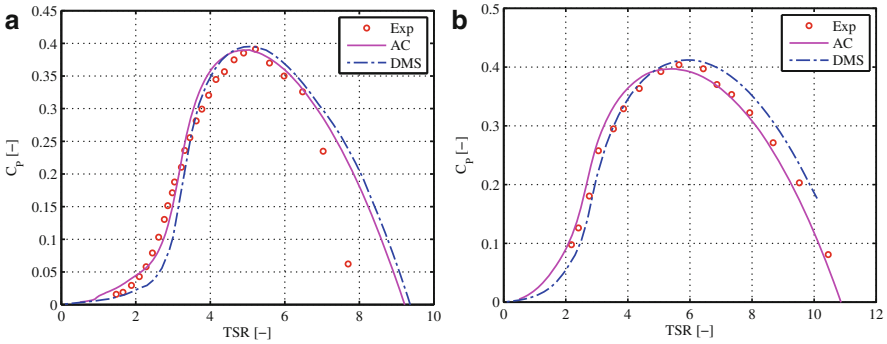

Fig. 12.4 Comparison of power coefficient curve between simulation model and experimental data. (**a**) The 3-bladed Sandia 5 m Darrieus rotor at rotational speed of 150 rpm, (**b**) the 2-bladed Sandia 17 m Darrieus rotor at rotational speed of 50.6 rpm

factor. The DMS model implemented by Wang et al. (2013) accounts for the effect of variation in the Reynolds number and incorporates the effect of dynamic stall using the Beddoes-Leishman dynamic stall model. It is validated by comparison with experimental results of the Sandia 5 m and 17 m Darrieus rotors, as shown in Fig. 12.4.

The AC method is a 2D quasi-steady flow model developed by Madsen (1982). The model extends the actuator disc concept to an actuator surface coinciding with the swept area of the 2D VAWT. In the AC model, the normal and tangential forces resulting from the blade forces are applied on the flow as volume force perpendicular and tangential to the rotor plane, respectively. The induced velocities are thus related to the volume force based on the continuity equation and Euler equation. The induced velocity includes a linear part and a nonlinear part; the linear part can be computed analytically given the normal and tangential loads. However, it's to some extent time-consuming to compute the nonlinear solution directly. A simple correction is therefore introduced to make the final solution in better agreement with the fully nonlinear solution. The developed AC model (Cheng et al. 2016a) is verified by comparison with other numerical models and experimental data, as demonstrated in Fig. 12.4. The AC model implemented in Cheng et al. (2016b) includes the effects of wind shear and turbulence, and dynamic inflow. The effect of dynamic stall is also incorporated using the Beddoes-Leishman dynamic stall model.

12.3.2 Hydrodynamics

The hydrodynamic loads are computed using a combination of the potential flow theory and Morison's equation. For large volume structures, the added mass, radiation damping and first order wave forces were obtained from a potential flow model

and applied in the time domain using the convolution technique (Faltinsen 1995). When the second-order wave force becomes important for structures with natural frequencies that either very low or near twice the wave frequency, the second-order potential flow theory is applied to account for the mean drift, difference-frequency and sum-frequency wave forces using the Newman approximation or quadratic transfer function (QTF). Regarding the slender structures where the diameter D is small compared to the wavelength λ (roughly, $D/\lambda < 1/5$), the Morison equation is applied to calculate the inertial load and viscous drag load (Faltinsen 1995). In addition, viscous forces on large volume structures can also be incorporated through the Morison's equation by considering only the quadratic viscous drag term.

12.3.3 Structural Dynamics

In the structural model, the blades are modeled as flexible beam elements with two symmetric planes to differ the flapwise stiffness and edgewise stiffness. The tower and shaft are modeled as axisymmetric beam elements while the mooring lines are considered as nonlinear bar element, as shown in Fig. 12.3. A flexible joint is used to connect the rotating part and non-rotating part within the shaft. The electric torque from the generator is also applied at this joint to regulate the rotor rotational speed according to the prescribed control strategy. Moreover, master–slave connections are applied to integrate the motions between the tower base and fairleads.

In RIFLEX, the dynamic equilibrium equations can be solved in the time domain using the Newmark-β numerical integration ($\beta = 0.256$, $\gamma = 0.505$). Structural damping is included through global proportional Rayleigh damping terms for all beam elements.

12.3.4 Control System

Considering a typical floating VAWT that operates at a fixed blade pitch angle, a generator torque controller can be used to regulate the rotational speed (Cheng et al. 2016b). The controller aims to minimize the error between the measured and filtered rotational speed Ω_{mea} and the reference rotational speed Ω_{ref} by adjusting the generator torque through a PI control algorithm.

For a typical floating VAWT system the relationship between the reference rotational speed and the wind speed is demonstrated in Fig. 12.5 (Cheng et al. 2016b). According to the operating conditions, it can be divided into three regions, as highlighted in Fig. 12.5. In region I where wind speeds ranges from V_{in} to $V_{\Omega N}$, the rotor operates at the optimal tip speed ratio so as to achieve the highest power coefficient. In region II, the rotor operates at a moderate tip speed ratio and holds the rotational speed constant at the rated one. The control targets in region I and II aim to maximize the power capture and at the same time keep the rotational speed

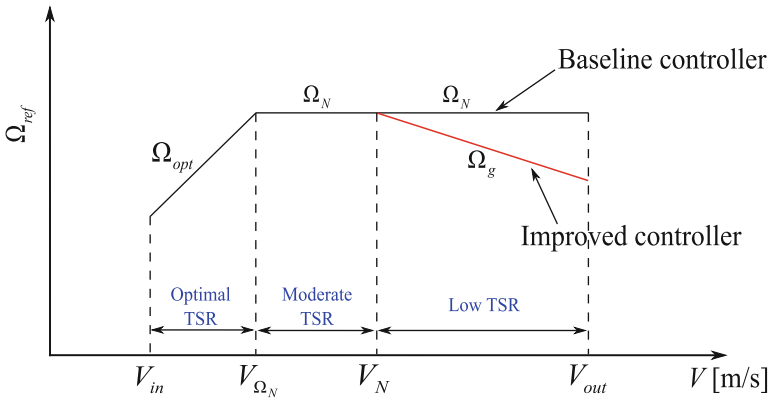

Fig. 12.5 The relationship between the reference rotor rotational speed and the wind speed for the baseline and improved controllers. V_{in}, V_N and V_{out} are the cut-in, rated, and cut-out wind speed, respectively; $V_{\Omega N}$ is the wind speed for the rated rotational speed; Ω_N is the rated rotational speed; Ω_{opt} is the optimal rotational speed that can maximize the power capture; Ω_g is the rotational speed that can hold the mean generator power approximately constant (Cheng et al. 2016b)

not larger than the rated one. However, the control targets in region III shift to limit the aerodynamic loads acting on the rotor by limiting the rotational speed. In this case, the rotor rotates at relatively low tip speed ratios and two control strategies, as illustrated in Fig. 12.5, are considered here.

Based on these two control strategies, two controller were developed, namely i.e. the baseline controller and improved controller. This baseline controller is capable of maximizing the power capture for wind speeds below $V_{\Omega N}$ and maintaining the rotational speed for wind speeds above $V_{\Omega N}$, while the improved controller aims to maximize the power capture for wind speeds below V_N and maintain the power capture approximately constant for the above rated wind speeds.

Both the baseline and improved controllers were implemented in the fully coupled codes. Figure 12.6 shows the mean generator power and thrust of a 5 MW Darrieus rotor with different controller. Above the rated wind speed, the improved controller successfully maintains the mean generator power approximately constant. Detailed information on the discrepancies between these two controllers is provided by Cheng et al. (2016b, 2016c).

12.3.5 Verification of the Fully Coupled Codes

The code SIMO-RIFLEX-DMS is developed by Wang et al. (2013) and verified by validating each module separately; the code SIMO-RIFLEX-AC is developed by Cheng et al. (2016b) and verified by a series of comparisons with the codes SIMO-RIFLEX-DMS and HAWC2. Considering an equivalent landbased 5 MW Darrieus rotor, these three codes are verified with each other by comparing the thrust, side force and aerodynamic torque in steady wind conditions, as shown in Figs. 12.7

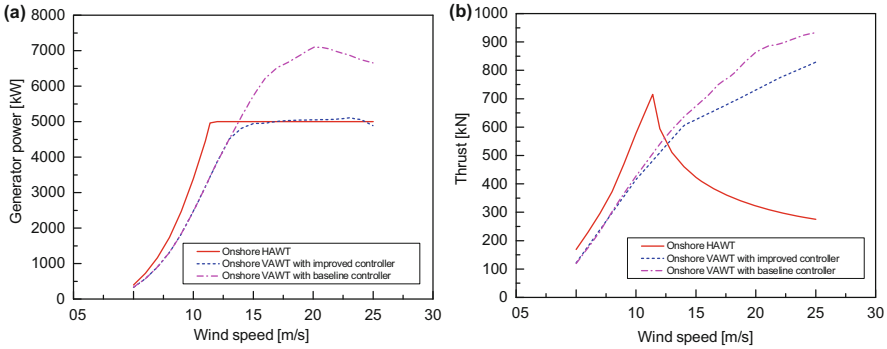

Fig. 12.6 Steady-state mean generator power and thrust of the onshore HAWT and VAWT with different control strategies (Cheng et al. 2016c)

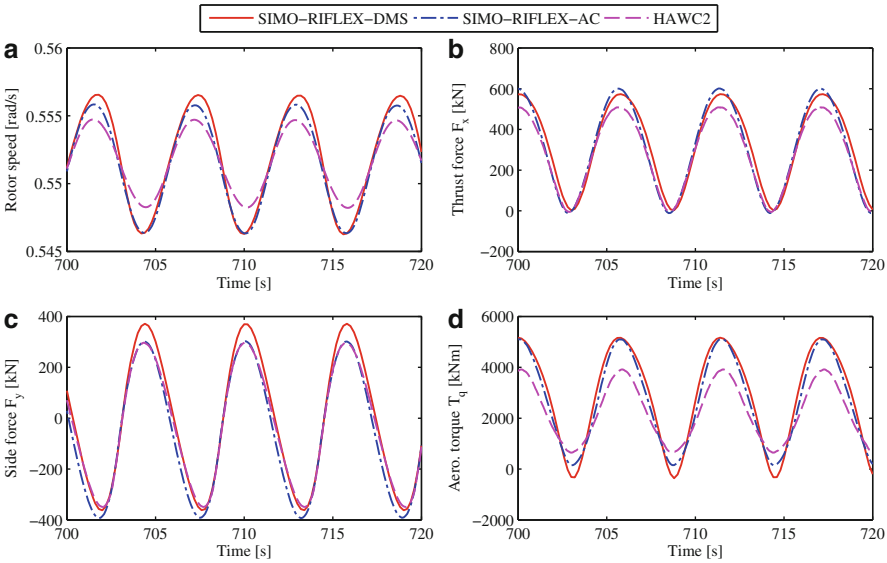

Fig. 12.7 Comparison of the rotational speed, thrust, side force and aerodynamic torque of the landbased VAWT using three codes without considering the effect of dynamic stall in the steady wind case with a wind speed of 8 m/s (Cheng et al. 2016b)

and 12.8. The load cases shown in these two figures correspond to a tip speed ratio of 4.39 and 2.51, which locate in region I and II as illustrated in Fig. 12.5, respectively. Here the effect of dynamic stall is not included since these three codes use different dynamic stall models. The developed codes SIMO-RIFLEX-DMS and SIMO-RIFLEX-AC are accurate enough in predicting the aerodynamic loads for landbased VAWTs. Essential differences among these three codes are also revealed and presented by Cheng et al. (2016b).

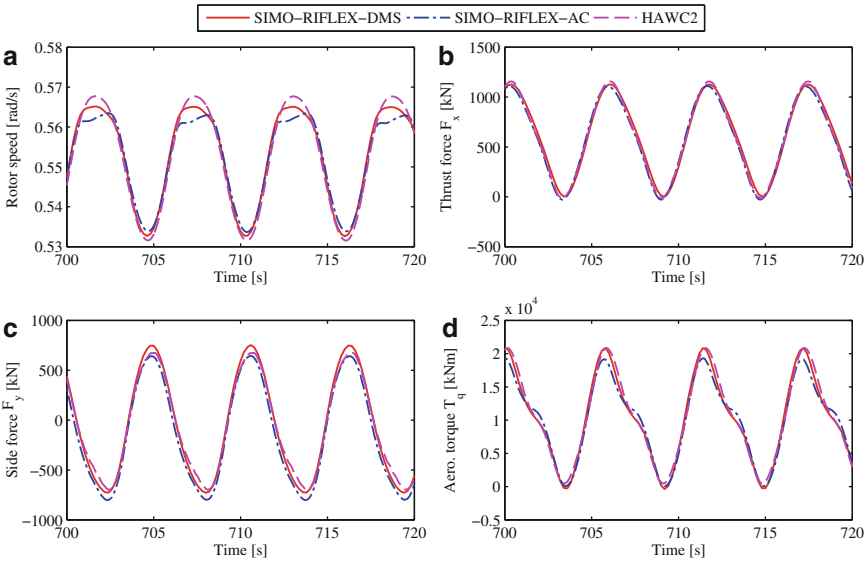

Fig. 12.8 Comparison of the rotational speed, thrust, side force and aerodynamic torque of the landbased VAWT using three codes without considering the effect of dynamic stall in the steady wind case with a wind speed of 14 m/s (Cheng et al. 2016b)

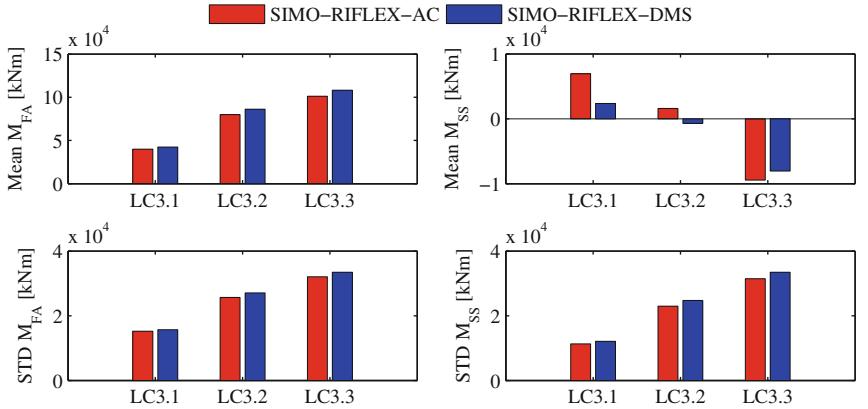

Fig. 12.9 Mean values and standard deviations of tower base fore-aft bending moment M_{FA} and side-side bending moment M_{SS} of the semi VAWT simulated using SIMO-RIFLEX-AC and SIMORIFLEX-DMS. The load cases are described by Cheng et al. (2016b)

In addition, the semi VAWT described in Sect. 12.2 is used to verify the capability of the codes SIMO-RIFLEX-DMS and SIMO-RIFLEX-AC in modeling and dynamic analysis of floating VAWTs. Figure 12.9 demonstrates the mean value and standard deviation of the tower base fore-aft and side-side bending moment for

the semi VAWT. It is found that the code SIMO-RIFLEX-AC can to some extent predict more accurate dynamic responses than the code SIMO-RIFLEX-DMS.

12.4 Dynamic Response Characteristics of Three Floating VAWTs

The stochastic dynamic responses of the three floating VAWT concepts (Cheng et al. 2015c), as described in Sect. 12.2, are studied under the turbulent wind and irregular wave conditions, including the generator power production, global platform motion, tower base fore-aft and side-side bending moments and tensions in mooring lines. The baseline controller is used during the simulations. Detailed descriptions of load cases used can be found in Cheng et al. (2015c). It should be noted that the stochastic dynamic responses in this section are calculated using the code SIMO-RIFLEX-DMS, and the results are plotted with the mean wind speed as the variable in the abscissa axis for simplicity.

Figure 12.10 shows the mean values of the generator power production of the three floating VAWT concepts. The error bar indicates the standard deviation from the mean value. It can be observed that the mean generator powers increase as the wind speed increases. At rated wind speed of 14 m/s, the mean generator powers slightly exceed the rated power of 5 MW, since the Beddoes-Leishman dynamic stall model is included in the DMS model. The rotor considered can achieve a rated power of 5 MW when excluding the dynamic stall effect. In addition, the mean

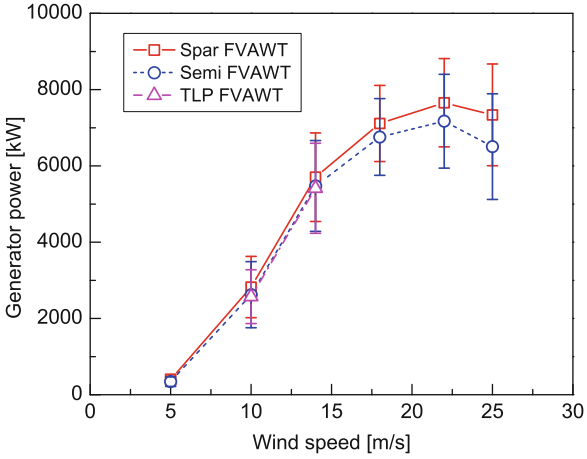

Fig. 12.10 Mean power production for the three floating VAWT concepts with error bar indicating the standard deviation from the mean value in the turbulent wind and irregular wave load cases. The load cases are indicated using mean wind speed in the abscissa axis. Results of the TLP VAWT are only given in load cases with wind speeds of 10 and 14 m/s (Cheng et al. 2015c)

generator power of the three floating VAWT concepts is very close to each other, except at high wind speeds where the mean generator power of the semi VAWT begins to differ from that of the spar VAWT. The difference results from the different rotational speed and increases as the wind speed increases. The different rotational speeds for the three concepts are due to the implemented controller. The controller regulates the rotational speed by adjusting the generator torque, but fails to keep the rotational speed at above rated wind speed exactly constant. The variations of the generator power for the three floating VAWT concepts are very close to each other as well.

The global platform motions of the three floating VAWT concepts present significant differences. The mean values of platform motions increase as the wind speed increases, since the mean values are mainly wind-induced. For each load case, the spar VAWT suffers the considerable larger platform motions in surge and pitch. But the standard deviations of the spar VAWT and semi VAWT in pitch motions are very close to each other. Regarding the yaw motion, the mean yaw motions of the three floating VAWT concepts are fairly close. However, the standard deviation of the yaw motion of the semi VAWT is relatively larger than that of the spar VAWT, this is due to the resonant yaw motions excited by the turbulent wind.

Characteristic structural responses for the three floating VAWT concepts are also of great interest. Here both the tower base fore-aft bending moment M_{FA} and side-side bending moment M_{SS} are chosen as the primary structural performance parameters. The tower base was assumed to be located below the bearings between the rotating shaft and the drive train shaft. Since the aerodynamic loads of each blade varies with the azimuthal angle, not only M_{FA} but also M_{SS} have great variations, which is quite different from the horizontal axis wind turbine. These variations of bending moments can cause large stress fluctuations, thus leading to great fatigue damage. Figure 12.11 compares the power spectra of M_{FA} and M_{SS} under the turbulent wind and irregular wave condition. The turbulent winds excite the certain low-frequency response of M_{FA}, but the wind-induced response is much smaller than the 2P response in both M_{FA} and M_{SS}. Furthermore, since the taut tendons cannot absorb the 2P aerodynamic excitations for the TLP VAWT, the 2P responses in M_{FA} and M_{SS} of the spar VAWT and semi VAWT are much smaller than that of the TLP VAWT, which implies that the catenary mooring system can greatly mitigate the 2P effects on structural dynamic responses. Eigen-frequency analysis has been carried out for this rotor and states that the natural frequencies of the first and second tower base bending modes are far away from the 1P and 2P excitations (Wang et al. 2013). As a consequence, the standard deviations of M_{FA} and M_{SS} for the spar VAWT and the semi VAWT are smaller than those of the TLP VAWT.

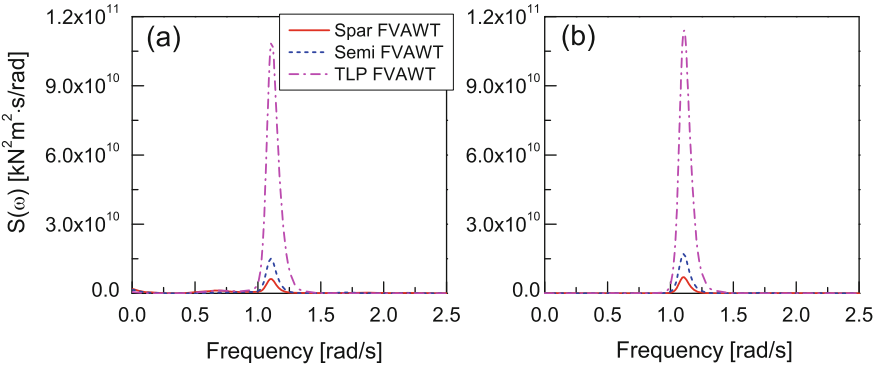

Fig. 12.11 Power spectra of tower base (**a**) fore-aft bending moment and (**b**) side-side bending moment for the three floating VAWT concepts in turbulent wind and irregular wave condition with $Uw = 14$ m/s, $Hs = 3.62$ m, $Tp = 10.29$ s

12.5 Comparative Study of Floating HAWTs and VAWTs

In this section, comparative studies on the dynamic responses of floating HAWTs and VAWTs are briefly discussed. The rotors considered are the NREL 5 MW wind turbine (Jonkman et al. 2009) and the 5 MW Darrieus rotor (Vita 2011). The code SIMO-RIFLEX-DMS and SIMO-RIFLEX-AeroDyn are used to conduct the fully coupled analysis for the floating VAWTs and HAWTs, respectively.

12.5.1 Semi HAWT vs. Semi VAWT

Wang et al. (2014b) studied the dynamics of the semi-type HAWT and VAWT with the OC4 semi-submersible supporting the NREL 5 MW wind turbine (Jonkman et al. 2009) and the 5 MW Darrieus rotor (Vita 2011). Regarding the semi VAWT, the baseline controller described in Sect. 12.3.4 was adopted in the simulations. Thus the generator power production of the semi VAWT exceeds 5 MW and is much larger than that of the semi HAWT above the rated wind speed. Other details with respect to the floating wind turbine systems and load cases can be found in Wang et al. (2014b).

The effect of 2P frequency on the structural responses, for instance the tower base bending moment, was identified for the semi VAWT. Moreover, power spectral analysis shows that the 2P response dominates the tower base fore-aft and side-side bending moment. Regarding the platform motions, the semi HAWT and VAWT have very close mean values and standard deviations in the pitch motion at low wind speeds. Power spectral analysis also reveals that the pitch motion of the semi VAWT has a smaller pitch resonant response and wave frequency response as well as a significantly notable 2P response, as demonstrated in Fig. 12.12.

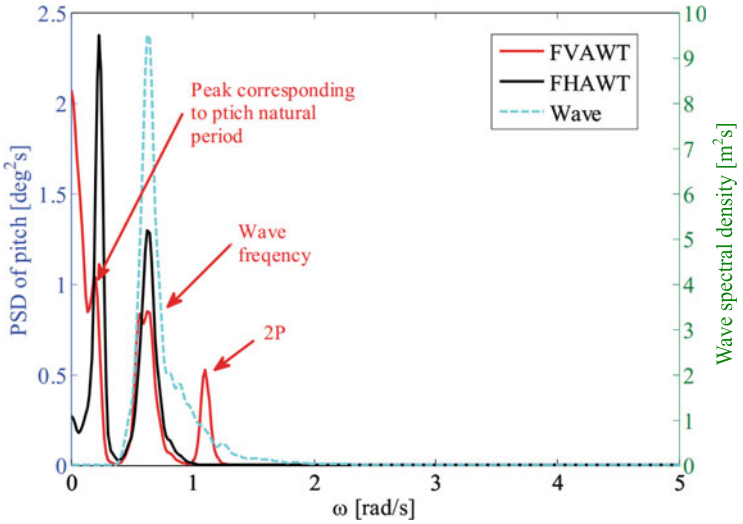

Fig. 12.12 Power spectra of the pitch motion of the semi HAWT and VAWT in turbulent wind and irregular wave condition with $Uw = 14$ m/s, $Hs = 3.62$ m, $Tp = 10.29$ s

12.5.2 Spar HAWT vs. Spar VAWT

Comparative study of floating HAWTs and VAWTs was further extended to the spar-type concepts by Cheng et al. (2015b, 2016c). The OC3 spar buoy was used to support the aforementioned two rotors. Cheng et al. (2015b) conducted the comparative study using the baseline control strategy for the spar VAWT. To make the comparative study more reasonable, an improved control strategy was employed, as described in Sect. 12.3.4 (Cheng et al. 2016c). A series of numerical simulations were carried out under the turbulent wind and irregular wave conditions.

Figure 12.13 shows the mean values and standard deviations of the generator power and thrust for the spar HAWT and VAWT. The response curves are plotted using the mean values with the error bar showing one standard deviation from the mean value. At wind speeds above 14 m/s, the mean generator powers of the spar HAWT and VAWT are very close to the rated power of 5 MW. However, the standard deviation of the generator power of the spar VAWT is approximately twice of that of the spar HAWT. For wind speeds below 14 m/s, the mean generator power of the spar HAWT is always much greater than that of the spar VAWT due to the higher power coefficient.

The spar HAWT and VAWT also differ in the platform motions due to the different aerodynamic loads and control strategies. For both the spar HAWT and VAWT, the trends in the mean values of the surge, heave and pitch are very similar to those of the mean thrust acting on the rotors, since the mean values of the platform motions are mainly related to wind thrust force. The mean values of the sway, roll

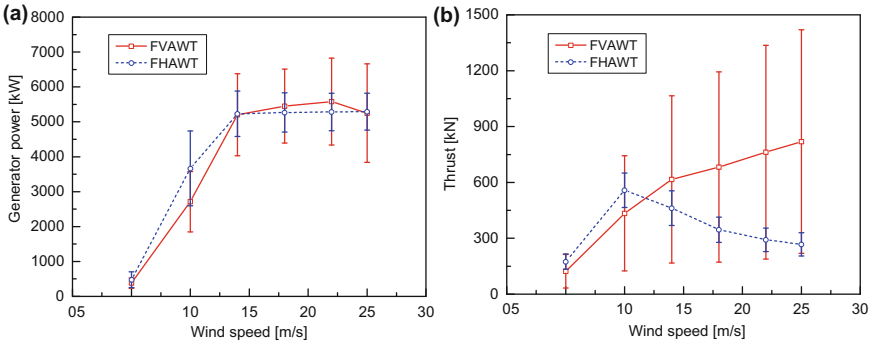

Fig. 12.13 Mean values and standard deviations of (**a**) generator power and (**b**) thrust for the spar type HAWT and VAWT under turbulent wind conditions. The error bar indicates the standard deviation

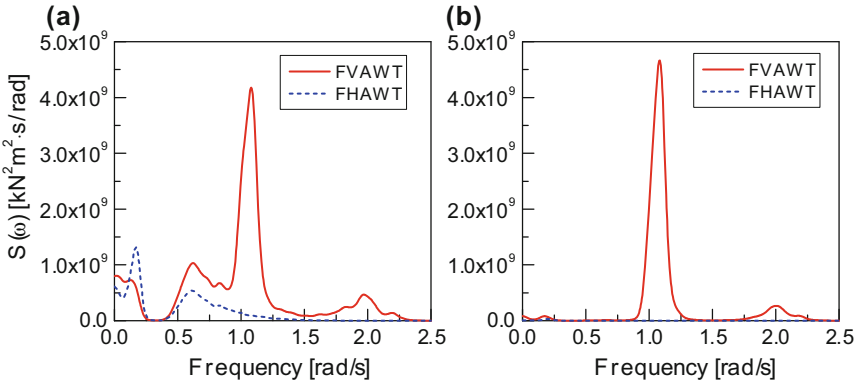

Fig. 12.14 Power spectra of the tower base (**a**) fore-aft bending moment and (**b**) side-side bending moment for the spar HAWT and VAWT in turbulent wind and irregular wave condition with $Uw = 14$ m/s, $Hs = 3.62$ m, $Tp = 10.29$ s

and yaw motions of the spar HAWT are very small, because the aerodynamic lateral force and yaw moment are small due to symmetry. However, the spar VAWT has much larger mean values in sway, roll and yaw motions, especially at high wind speed.

The structural responses of the spar HAWT and VAWT illustrate significant differences as well. Figure 12.14 shows the power spectra of the tower base fore-aft and side-side bending moment for the spar HAWT and VAWT in turbulent wind and irregular wave condition with Uw = 14 m/s, Hs = 3.62 m, Tp = 10.29 s. Obviously the response corresponding to the 2P frequency is considerably dominating in the tower base fore-aft and side-side bending moments for the spar VAWT. Moreover, the tower base fore-aft bending moment for the spar VAWT also includes prominent low-frequency turbulent wind induced response and wave frequency response. With respect to the spar HAWT, the tower base fore-aft bending moment consists of

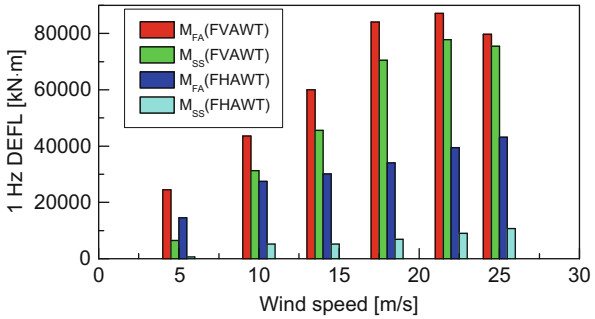

Fig. 12.15 1 Hz damage equivalent fatigue loads (DEFLs) of the tower base fore-aft bending moment (M_{FA}) and side-side bending moment (M_{SS}) for the spar HAWT and VAWT

significant low-frequency turbulent wind induced response, pitch resonant response and wave frequency response. The pitch resonant response mainly results from the relatively large platform pitch motion. In addition, the tower base of the spar HAWT is mainly affected by the fore-aft bending moment, while the side-to-side bending moment can be neglected.

The tower base of the spar VAWT will suffer relatively larger fatigue damage than that of the spar HAWT, as shown in Fig. 12.15. A Matlab-based computer program MLife developed by NREL (Hayman 2012) is used to estimate the short-term damage equivalent fatigue loads (DEFLs). The DEFL of the fore-aft bending moment for the spar VAWT above the rated wind speed is approximately twice that of the spar HAWT. Moreover, the DEFL of the side-side bending moment for the spar VAWT is more than six times greater than that of the spar HAWT.

12.6 Conclusions

This paper deals with the integrated modeling methodology for a floating vertical axis wind turbine (VAWT) system and reveals the dynamic response characteristics of representative floating VAWTs.

Firstly two fully coupled simulation tools, namely SIMO-RIFLEX-DMS and SIMO-RIFLEX-AC, are briefly introduced so as to assess the dynamic performance of typical floating VAWT concepts. These two simulation tools are based on the double multi-streamtube (DMS) method and actuator cylinder (AC) flow method, respectively. Moreover, they are capable of accounting for the turbulent inflow, aerodynamics, hydrodynamics, structural elasticity and controller dynamics. Validations of the aerodynamic module using experimental data and verifications of the fully coupled tools using a series of code-to-code comparisons are also presented.

The dynamic responses of three floating VAWT concepts are then studied. A spar, semi-submersible and TLP floater is used to support a two-bladed Darrieus rotor, respectively. Stochastic dynamic response analysis reveals that 2P effects resulting from the 2P aerodynamic loads are prominent in the dynamic responses of these concepts. Due to the compliant catenary mooring systems, the spar and the semi-submersible can help to mitigate the 2P effects on structural loads and mooring line tensions as compared to the TLP concept, at the cost of larger platform motions. The TLP is not a good substructure for vertical axis wind turbine unless the cyclic variation of aerodynamic loads is significantly reduced.

Comparative studies on the dynamics of floating VAWTs and HAWTs are also demonstrated. Due to different aerodynamic load characteristics and control strategies, the spar VAWT results in larger mean tower base bending moments and mooring line tensions above the rated wind speed. Because significant 2P aerodynamic loads act on the spar VAWT, the generator power, tower base bending moments and delta line tensions show prominent 2P variation. Consequently the spar VAWT suffers severe fatigue damage at the tower bottom. The semi VAWT shows significant 2P variations in structural responses as well.

Acknowledgments The authors would like to acknowledge the financial support from the EU FP7 project MARE WINT (project NO. 309395) and Research Council of Norway through the Centre for Ships and Ocean Structures (CeSOS) and Centre for Autonomous Marine Operations and Systems (AMOS) at the Department of Marine Technology, Norwegian University of Science and Technology (NTNU), Trondheim, Norway. The first author would also thank Dr. Kai Wang from Aker Solutions for his valuable comments and discussions.

References

Akimoto H, Tanaka K, Uzawa K (2011) Floating axis wind turbines for offshore power generation–a conceptual study. Environ Res Lett 6(4):044017. doi:10.1088/1748-9326/6/4/044017

Borg M, Collu M (2014) A comparison on the dynamics of a floating vertical axis wind turbine on three different floating support structures. Energy Procedia 53:268–279. doi:10.1016/j.egypro.2014.07.236

Borg M, Collu M, Brennan FP (2013) Use of a wave energy converter as a motion suppression device for floating wind turbines. Energy Procedia 35:223–233. doi:10.1016/j.egypro.2013.07.175

Borg M, Collu M, Kolios A (2014a) Offshore floating vertical axis wind turbines, dynamics modelling state of the art. Part II: mooring line and structural dynamics. Renew Sustain Energy Rev. doi:10.1016/j.rser.2014.07.122

Borg M, Shires A, Collu M (2014b) Offshore floating vertical axis wind turbines, dynamics modelling state of the art. Part I: aerodynamics. Renew Sustain Energy Rev. doi:10.1016/j.rser.2014.07.096

Borg M, Wang K, Collu M et al (2014c) A comparison of two coupled model of dynamics for offshore floating vertical axis wind turbines (VAWT). Paper presented at the 33rd international conference on ocean, offshore and arctic engineering, ASME, San Francisco, 8–13 June 2014

Cahay M, Luquiau E, Smadja C (2011) Use of a vertical wind turbine in an offshore floating wind farm. Paper presented at the offshore technology conference, Houston, 2–5 May 2011

Cheng Z, Wang K, Gao Z et al (2015a) Dynamic modelling and analysis of three floating wind turbine concepts with vertical axis rotor. In: Chung JS, Vorpahl F, Hong SY et al (eds) The proceedings of the 25th (2015) international ocean and polar engineering conference, Kona, June 2015. ISOPE, California, p 415

Cheng Z, Wang K, Gao Z et al (2015b) Comparative study of spar type floating horizontal and vertical axis wind turbines subjected to constant winds. Paper presented at the Offshore 2015. European Wind Energy Association, Copenhagen, 10–12 March 2015

Cheng Z, Wang K, Gao Z, Moan T (2015c) Dynamic response analysis of three floating wind turbine concepts with a two-bladed Darrieus rotor. J Ocean Wind Energy 2(4):213–222. doi:10.17736/jowe.2015.jcr33

Cheng Z, Madsen HA, Gao Z et al (2016a) Aerodynamic modeling of floating vertical axis wind turbines using the actuator cylinder method. Submitted to Energy Procedia

Cheng Z, Madsen HA, Gao Z, Moan T (2016b) A fully coupled method for numerical modeling and dynamic analysis of floating vertical axis wind turbines. Submitted to Renewable Energy

Cheng Z, Wang K, Gao Z, Moan T (2016c) A comparative study on dynamic responses of spar-type floating horizontal and vertical axis wind turbines. Wind Energy (accepted)

Collu M, Borg M, Shires A et al (2013) FloVAWT: progress on the development of a coupled model of dynamics for floating offshore vertical axis wind turbines. Paper presented at the 32nd international conference on ocean, offshore and arctic engineering, ASME, Nantes, 9–14 June 2013

Dabiri JO (2011) Potential order-of-magnitude enhancement of wind farm power density via counter-rotating vertical-axis wind turbine arrays. J Renew Sustain Energy 3(4):043–104. doi:10.1063/1.3608170

Faltinsen OM (1995) Sea loads on ships and offshore structures. Cambridge University Press, Cambridge

Hayman G (2012) Mlife theory manual for version 1.00. In: National Renewable Energy Laboratory National Wind Technology Center (NWTC) Information Portal. Available via NWTC. https://nwtc.nrel.gov/system/files/MLife_Theory.pdf. Accessed 09 Apr 2016

Jonkman JM, Butterfield S, Musial W et al (2009) Definition of a 5-mw reference wind turbine for offshore system development: Tech. Rep. NREL/TP-500-38060. In: NREL publications. Available via NREL. http://www.nrel.gov/docs/fy09osti/38060.pdf. Accessed 09 Apr 2016

Larsen TJ, Madsen HA (2013) On the way to reliable aeroelastic load simulation on VAWT's. Paper presented at the European Wind Energy Conference and Exhibition (EWEA), Austria, 4–7 February 2013

Luxcey N, Ormberg H, Passano E (2011) Global analysis of a floating wind turbine using an aero-hydro-elastic numerical model: Part 2: benchmark study. Paper presented at the ASME 2011, 30th international conference on ocean, offshore and arctic engineering, Rotterdam, 19–24 June 2011

Madsen HA (1982) The actuator cylinder: a flow model for vertical axis wind turbines. Technical Report, Institute of Industrial Constructions and Energy Technology, Aalborg University Centre, Aalborg

MARINTEK (2012a) RIFLEX theory manual, version 4.0. Norwegian Marine Technology Research Institute, Trondheim

MARINTEK (2012b) SIMO theory manual version 4.0. Norwegian Marine Technology Research Institute, Trondheim

Ormberg H, Passano E, Luxcey N (2011) Global analysis of a floating wind turbine using an aero-hydro-elastic model: Part 1 code development and case study. Paper presented at the ASME 2011, 30th international conference on ocean, offshore and arctic engineering, Rotterdam, 19–24 June 2011

Owens B, Hurtado JE, Paquette JA et al (2013) Aeroelastic modeling of large off-shore vertical-axis wind turbines: development of the offshore wind energy simulation toolkit. Paper presented at the 54th AIAA/ASME/ASCE/AHS/ASC structures, structural dynamics and materials co-located conferences, Boston, 8–11 April 2016

Paquette J, Barone M (2012) Innovative offshore vertical-axis wind turbine rotor project. Paper presented at the EWEA 2012 annual event, Copenhagen, 16–19 April 2012

Paraschivoiu I (2002) Wind turbine design: with emphasis on Darrieus concept. Polytechnic International Press, Montreal

Paulsen US, Madsen HA, Hattel JH et al (2013) Design optimization of a 5 mw floating offshore vertical-axis wind turbine. Energy Procedia 35:22–32. doi:10.1016/j.egypro.2013.07.155

Vita L (2011) Offshore floating vertical axis wind turbines with rotating platform. Dissertation, Technical University of Denmark

Wang K, Moan T, Hansen MOL (2013) A method for modeling of floating vertical axis wind turbine. Paper presented at the 32nd international conference on ocean, offshore and arctic engineering, ASME, Nantes, 9–14 June 2013

Wang K, Hansen MOL, Moan T (2014a) Dynamic analysis of a floating vertical axis wind turbine under emergency shutdown using hydrodynamic brake. Energy Procedia 53:56–69

Wang K, Luan C, Moan T et al (2014b) Comparative study of a FVAWT and a FHAWT with a semi-submersible floater. In: Chung JS, Vorpahl F, Hong SY et al (eds) The proceedings of the 24th (2014) international ocean and polar engineering conference, Busan, June 2014. ISOPE, California, p 302

Wang K, Cheng Z, Moan T et al (2015a) Effect of difference-frequency forces on the dynamics of a semi-submersible type FVAWT in misaligned wave-wind condition. In: Chung JS, Vorpahl F, Hong SY et al (eds) The proceedings of the 25th (2015) international ocean and polar engineering conference, Kona, June 2015. ISOPE, California, p 517

Wang K, Hansen MOL, Moan T (2015b) Model improvements for evaluating the effect of tower tilting on the aerodynamics of a vertical axis wind turbine. Wind Energy 18:91–110. doi:10.1002/we.1685

Wang K, Moan T, Hansen MOL (2016) Stochastic dynamic response analysis of a floating vertical-axis wind turbine with a semi-submersible floater. Wind Energy. doi:10.1002/we.1955

Chapter 13
Bottom Fixed Substructure Analysis, Model Testing and Design for Harsh Environment

Duje Veic, Marek Kraskowski, and Tomasz Bugalski

Abstract The aim of this chapter is to study the various hydrodynamic loads important for the design process of offshore wind turbines foundations. A numerical study on weakly non-linear waves was conducted, using the commercial code StarCCM++. Open-source codes OpenFoam and OceanWave3D were used for the simulation of breaking waves. Existing analytical and empirical formulations, and the results and conclusions from the current numerical study are presented.

13.1 Introduction

The main objective of this study is load analysis on fixed bottom support structures of offshore wind turbines suitable for shallow waters and transitional depths (up to 60 m). Usually, hydrodynamic loads cause lower impact on the tower deflection than the wind loads, however for some conditions hydrodynamic loads excite the structure more severely. Hydrodynamic loads are subject of the study in this research, with the primary focus on impulse forces from the breaking waves.

Quantitative data collection from model tests in the AQUILO[1] project is used for the study on wave propagation and wave loads in the numerical wave tank, by using commercial code StarCCM++. Furthermore, empirical solutions from the Morison equation (Morison et al. 1950) are compared with experimental data as well. Experiments were conducted on support structures installed in the intermediate water depths (d = 40–60 m).

[1] AQUILO—Development of the selection method of the offshore wind turbine support structure for Polish maritime areas, project cofounded by NCBiR; www.morceko-aquilo.pl

D. Veic (✉) • M. Kraskowski • T. Bugalski
Centrum Techniki Okrętowej S.A. (Ship Design and Research Centre S.A.), ul. Szczecińska 65, 80-392 Gdańsk, Poland
e-mail: dujeveic@gmail.com; marek.kraskowski@cto.gda.pl; tomasz.bugalski@cto.gda.pl

W. Ostachowicz et al. (eds.), *MARE-WINT*, DOI 10.1007/978-3-319-39095-6_13

Collaboration with Deltares/Delft within the framework of WiFi[2], allowed for an insight into comprehensive experimental data for validation of numerical open-source codes—OpenFoam and OceanWave3D. Experiments were conducted on a monopile structure installed in relatively shallow water (d = 30 m). A series of impulse loadings from breaking waves were observed. It is expected that more comprehensive results will be published after completion of the research. In this chapter, a part of the numerical study is presented.

In short, the purpose of this paper is to present the types of hydrodynamic loads important for the design process of offshore wind turbines foundations, to give a note on existing analytical and empirical formulations and to present results and conclusions from the numerical study.

13.2 Determination of Design Wave

Regular wave profiles in deep water, or intermediate water depth that is not too steep, follow a sinusoidal shape and are well described by linear wave theory. As wave height increases and water depth decreases the wave crest tends to become more narrow and steep, whereas the wave trough becomes long and flat. This happens as the wave starts to sense the bottom. Nonlinearity of wave increases with increased steepness of the wave. Weakly non-linear, undisturbed waves are in general well understood, and higher order perturbation solutions—such as Stokes 3rd, Stokes 5th, and fully non-linear stream function theories—exist for regular waves.

Figure 13.1 shows regions of recommended wave theories. Near the point of breaking, a wave becomes highly nonlinear, and at the point of breaking releases a high amount of energy; such events can have a significant contribution on the loading of offshore wind turbines.

Sea states are approximated by wave spectra. The Pierson-Moskowitz (Pierson and Moskowitz 1964) and JONSWAP spectrum are commonly used in practice. Generally, the point of interest is the maximum wave elevation in a 3 h storm duration which may occur once in 50-years. Within that duration, the maximum expected wave height can be estimated as $H_{max} = 1.86H_s$ (DNV 2014), where H_s is significant wave height.

Marked positions on Fig. 13.1 correspond to representative cases from experiments in the AQUILO and WiFi projects. Figure 13.2 presents comparison between experimentally observed wave elevation just before wave breaking and theoritical estimations.

[2]WiFi—joint industry project, Wave Impact on Fixed turbines; secondment at Del-tares/Delft.

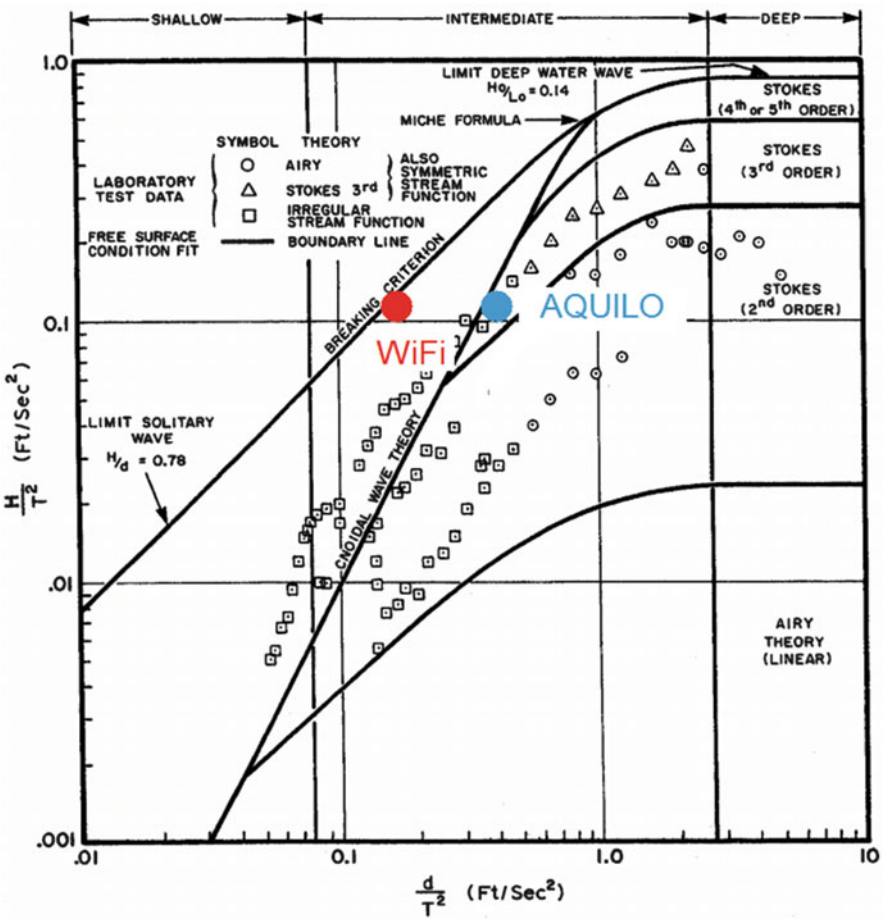

Fig. 13.1 Recommended wave theories (*Source*: DNV 2014)

13.3 Hydrodynamic Loads

The rotor thrust reaction to wind loads acts on a larger lever arm than loads from the waves. Usually, hydrodynamic loads cause a smaller impact on the tower deflection than wind loads. Wind loads are a dominant source of fatigue loading; however in cases when wind and waves are misaligned, there is no influence of aerodynamic damping, and fatigue from hydrodynamic loads has to be taken into consideration as well.

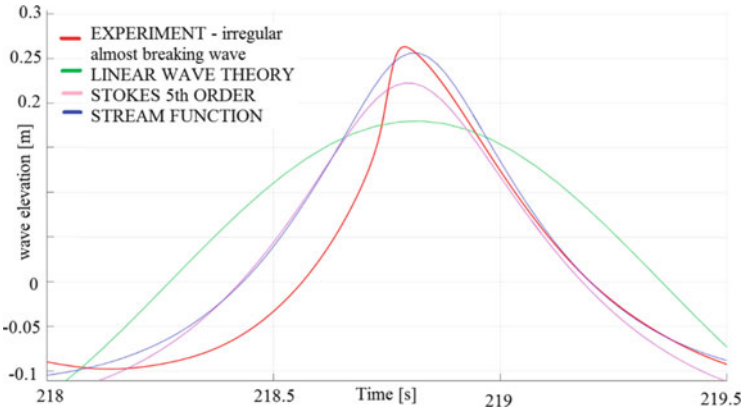

Fig. 13.2 Wave elevation time trace; comparison experiment-theories

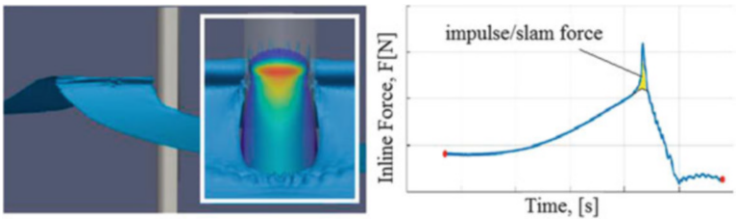

Fig. 13.3 Breaking wave impact (slam) force

Typical design drivers for foundations of offshore wind turbines are impact forces from very steep and breaking waves (Fig. 13.3), which can be expected at sites where monopile support structures are usually installed (in up to 30 m water depth).

The extreme and fatigue response stresses depend strongly on the dynamic behavior of the wind turbine structure. When harmonics of the wave frequency coincide with the natural frequency of the structure, the resonance of the structure may result in an amplification of the response. The foundations of fixed bottom wind turbines are designed such that the natural frequency of the structure is out of the range of wave spectrum frequencies. However, higher harmonics of wave excitation can excite structures in resonance and thus amplify the total response. In literature, the phenomena of “ringing” and “springing” are associated with higher harmonic excitations from the incident wave (Faltinsen 1993).

13.4 Analytical and Empirical Formulations

13.4.1 Morison Equation

The Morison equation (Morison et al. 1950) is by far the most used equation for computing wave loads on slender structures such as jackets and monopiles. The inline force on a slender body is estimated from fluid velocities and accelerations. The Morison equation is a sum of two terms; one being an empirical drag term proportional to the fluid velocity squared, and the other being an inertia term, derived from potential flow theory, proportional to the fluid acceleration. The Morison equation is defined as follows:

$$F = {}^{1}\!/_{2}\, C_d \rho D \left|U\right| U + C_m \rho A \left|\dot{U}\right| \tag{13.1}$$

The empirical force coefficients C_m and C_d in the Morison's equation are determined from 2D experiments. In general, the drag and inertia coefficients are functions of the Reynolds number, the Keulegan-Carpenter number, the relative roughness, and the ratio between waves and current. The Morison equation which is based on a stream function wave theory predicts the loadings of weakly non-linear waves with good accuracy.

13.4.2 Higher Harmonic Forces

An amplification of the structural response can be expected when higher harmonics of non-linear waves coincide with the 1st structural natural frequency. The "Ringing" phenomenon is usually associated with third harmonic excitations from incident waves. The reason why the third harmonic force and "ringing" responses are often associated is that $f_{tower}/3$ is close to typical peak frequencies of storm waves (Paulsen 2013). When a "ringing" phenomenon is expected, it has to be considered in the design process of wind turbine foundations (DNV 2014).

A comprehensive literature review and a study on higher harmonic loads can be found in the work of (Paulsen 2013). Paulsen (2013) studied higher harmonic loads numerically and compared the obtained results with third order perturbation theories from Faltinsen (1993) and Malenica and Molin (1995). The study by Paulsen (2013) also compared results with the Morison equation with an additional term proposed by Rainey (1989).

13.4.3 Impulse (Slam) Forces from Breaking Waves

Plunging wave breakers can excite the structure most violently. For the calculation of the impact forces on slender structures, an additional part in the Morison equation is introduced:

$$F = F_{Morison} + F_{slam} = F_{inertia} + F_{drag} + F_{slam} \tag{13.2}$$

where F_{slam}[N] is the slam force, defined as the integration of inline impact force, f_i[N/m], over the area of the impact (Fig. 13.4):

$$F_{slam} = \int_0^{area} f_i = \eta_b \lambda' * fi \tag{13.3}$$

$$F_{slam} = \eta_b \lambda * fi; \text{ rectangular force distribution} \tag{13.4a}$$

$$F_{slam} = 0.5\eta_b \lambda * fi; \text{ triangular force distribution} \tag{13.4b}$$

The parameter which indicates how much of the wave crest (η_b[m]) is active in the impulse force is defined as the "curling factor" (λ).

The line impact force is generally defined as:

$$f_i = C_s(t)\rho R C_b{}^2 \tag{13.5}$$

where Cs is defined as the "slamming coefficient".

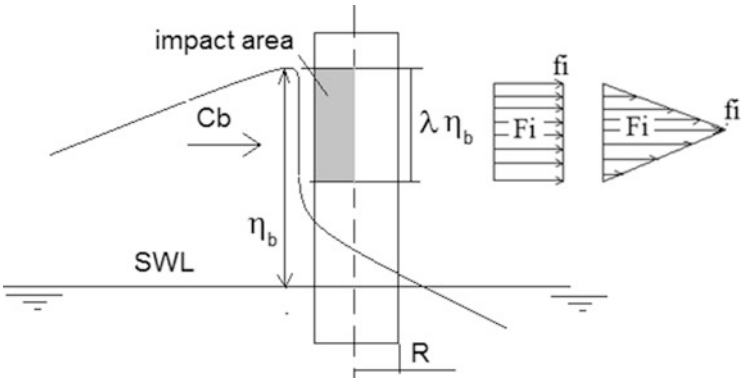

Fig. 13.4 Breaking wave parameters

Studies on impact forces from breaking waves are usually compared with one of the first studies on wave entry problems done by Von Karman (1929) and Wagner (1932). They studied impact forces for a case when an infinitely long falling cylinder hits a calm water surface. The cylinder was approximated as a flat plate. Von Karman (1929) considered the momentum conservation during the impact as:

$$f_i = d\left(m_h V\right)/dt \tag{13.6}$$

where $m_h = 0.5\pi\rho c^2$ is the added mass below the flat plate.

Wagner (1932) considered the velocity potential around a flat plate as:

$$\phi = -V\sqrt{c(t)^2 - x^2} \tag{13.7}$$

and by estimating $c(t) = 2\sqrt{VtR}$, he solved temporal part of the Bernoulli's equation. Wagner (1932) also explained the so-called "pile-up" effect, which is the deformation of the water free surface around the plate. Due to this "pile-up effect", the immersion of the cylinder occurs earlier. As a result, the duration of the impact decreases and the maximum impact force increases. Thus, the force calculated by applying Wagner's theory is estimated as twice the line force calculated by von Karman's theory (Table 13.1). Both theories are time independent and present only a maximum line force.

For the calculation of impact forces due to plunging wave breakers on offshore wind turbines, a reference is usually made to the model developed by Wienke and Oumeraci (2005). The theoretical description of their model is based on Wagner's (1932) 2D-model; to account for the temporal development of the impact they compute the non-linear velocity term in Bernoulli's equation.

Comprehensive experimental studies have been conducted to study impact forces of breaking waves. High fluctuations and scattering from the point of view of local

Table 13.1 Overview on wave impact studies

Author	Max inline force (ρRc^2)		Max press (ρc^2)	
von Karman (1929)	π	T		
Wagner (1932)	2π	T		
Goda et al. (1966)	π	T		
Sawaragi and Nochino (1984)	3π	E		
Tanimoto et al. (1987)	1.1π–1.8π	E		
Zhou et al. (1991)			4–13	E
Chaplin (1993)	2π–4π	E		
Chan et al. (1995)			16–47	E
Wienke and Oumeraci (2005)	2π	T	40	E
Ros (2011)	1.1π–1.4π	E		
Hildebrandt and Schlurmann (2012)	0.8π–1.1π	N	4–12.5	E

T theory, *E* experiment, *N* numerical

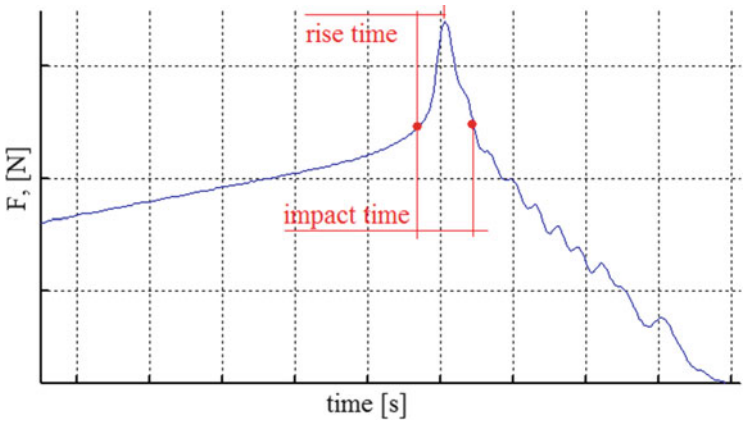

Fig. 13.5 Force signal

line forces and local pressures are observed. Table 13.1 gives an overview on wave impact studies.

The nature of impulsive forces is characterized by very short durations, and the resulting structural responses are sensitive to dynamic analysis; hence, both the intensity and the time history of impact (slamming) forces are important design parameters. The total impact duration and the "rising time", are both important parameters for dynamic structure analysis (Fig. 13.5).

13.5 Numerical Analysis

The Navier–Stokes equations can be solved in combination with volume of fluid (VOF) surface capturing scheme. For an incompressible two phase flow, conservation of mass and momentum in an Eulerian frame of reference, is given by:

$$\nabla \cdot \mathbf{u} = 0 \tag{13.8}$$

$$\frac{\partial}{\partial t}\rho\mathbf{u} + \rho\left(\nabla\mathbf{u}\right)\mathbf{u} = -\nabla p^{*} - \left(\mathbf{g}\cdot\mathbf{x}\right)\nabla\rho + \nabla\rho\left(\boldsymbol{\mu}\nabla\mathbf{u}\right) \tag{13.9}$$

where $\mathbf{u} = (u, v, w)$ is the instantaneous velocity in Cartesian coordinates, ρ is the density, p^{*} is the pressure in excess of the hydrostatic pressure, $\mathbf{g}$ is the acceleration due to gravity, $\mathbf{x}$ is the Cartesian coordinate vector, μ is the dynamic molecular viscosity.

The free surface separating the air and water phase is captured using a VOF surface capturing scheme, which solves the following equation for the water volume fraction (α):

$$\frac{\partial \alpha}{\partial t} + \nabla \cdot \mathbf{u}\alpha + \nabla \cdot \mathbf{u}_r \alpha (1 - \alpha) = 0 \tag{13.10}$$

In Eq. (13.10), $\mathbf{u}_r$ is a relative velocity (Berberović et al. 2009), which helps to retain a sharp interface, and the term $\alpha (1 - \alpha)$ vanishes everywhere except at the interface. The marker function is 1 when the computational cell is filled with water, and 0 when it is empty; in the free surface zone, the marker function will have a value in the interval $\alpha \in [0; 1]$ indicating the volume fraction of water and air respectively. The fluid density and viscosity is assumed continuous and differentiable in the entire domain, and the following linear weighting of the fluid properties is adopted:

$$\rho = \alpha \rho_w + (1 - \alpha) \rho_a; \ \mu = \alpha \mu_w + (1 - \alpha) \mu_a \tag{13.11}$$

In Eq. (13.9), the sub-indices w and a refer to water and air respectively.

13.5.1 Star CCM++

Numerical analyses within the framework of the AQUILO project were done by using the commercial CFD package StarCCM++. Sensitivity analyses on the regular wave propagation in the numerical domain were also conducted. The inlet boundary condition in the computations is based on the free surface elevation and the velocity components are calculated according to desired wave, using the corresponding wave theory. Wave theories up to the Stokes 5th order theory are implemented in the StarCCM++ package. Waves examined in the scope of the AQUILO can be described as a weakly non-linear and they are well estimated by the Stokes 5th order regular wave theory (Fig. 13.1). The sensitivity of mesh parameters, time step, discretization method and turbulence model was investigated. It was ensured that the reflections from the boundaries were neutralized. The following conclusions were drawn:

- The domain should be refined in the free surface zone (around 25 cells per wave height and 115 cells per wave length); the aspect ratio should be $dx/dz \leq 4$ (Fig. 13.6)
- Second order time discretization should be used with at least five iterations per time step; in the equation for volume fraction of water, the convection flux was discretized using a special high-resolution interface-capturing (HRIC) scheme which is designed to keep the interface sharp. To use the HRIC scheme propagation, the wave should be less than half a cell per time step

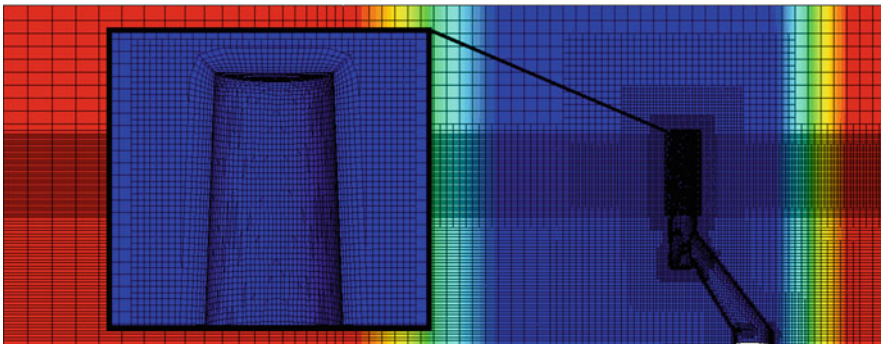

Fig. 13.6 Part of the numerical domain domain, grid refinement

- k-ε turbulence models introduce significant generation of eddy viscosity at the free surface interface; significant numerical diffusion was observed. After wave propagation of few wave lengths, wave height was reduced up to the 20 % compared with the initialized wave height.
- Better results were obtained by using an inviscid model. After wave propagation of 20 wave lengths, the wave height was reduced up to the 6 % compared to the initialized wave height
- The structure under analysis must not be placed too close to the inlet boundary because of the reflected waves that propagate upstream toward the inlet boundary and changing inlet values.
- In a case where the linear wave propagating in the numerical tank is influenced by the sea bed, the obtained wave height at the position of interest was around 20 % lower than theoretically expected.
- It was found that the propagation of a wave, influenced by the sea bed, suffers from significant damping. It is suggested that parameters of initialised wave be close to the characteristics of the specific wave of interest.

As waves under the consideration in the AQUILO project are well approximated by Stokes 5th order theory (which is also implemented in the StarCCM++), a "forcing" technique for the further analysis. In the "forcing" technique, the idea is to have free zone around the structure of the interest while, in the rest of the domain, solutions are forced towards theoretical solutions (Fig. 13.7). At each time step, if the solution differs from the theoretical solution it is "forced" towards theoretical solution by assuming an additional source in the transport equation. The additional term in the transport equation is defined as:

$$b_\phi = -\lambda \left(\phi - \phi^*\right) \tag{13.12}$$

where λ is forcing coefficient; ϕ is the solution of the transport equation at the given CV centroid; and $\phi^*$is the value towards which the solution is forced. This technique is used with very large values of λ, when the solution needs to be fixed

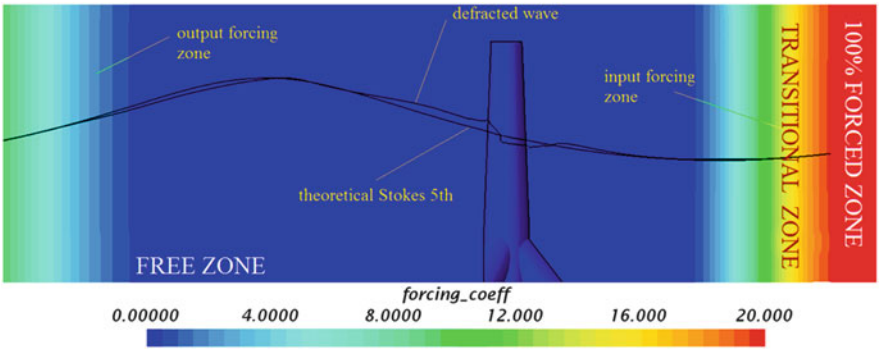

Fig. 13.7 "Forcing" technique

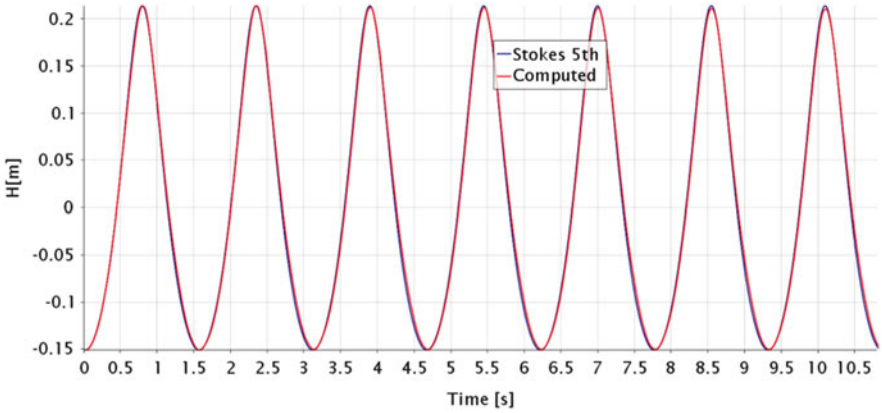

Fig. 13.8 Comparison between theoretical and computational results

to a certain value—after which then the remaining parts of the discretized equation become negligible.

In this technique, waves that are reflected off the structure and propagate upstream towards inlet boundary can be reduced and their influence on results can be eliminated; additionally, the necessary wave damping towards the outlet can be achieved more progressively, and the domain size can be reduced so that the speed of computation is increased.

An almost perfect comparison between the theoretical and numerical computations is presented in Fig. 13.8. As the Stokes 5th order wave theory is the highest wave theory implemented in STAR CCM++, theoretical solutions from other sources need to be employed for an analysis of steeper, strongly non-linear waves.

13.5.2 OceanWave3D: OpenFoam

To correctly predict the nonlinearity of the incident waves, bathymetry changes have to be taken into account as soon as the wave starts to get influenced by the bottom. To simulate the propagation of a wave with a strong influence of the sea bed (very steep, near breaking or breaking waves) the computation domain should be very long—however, the solution would be significantly influenced by numerical diffusion. To reduce the influence of numerical diffusion, and to reduce the time of the computation, one can solve the Navier–Stokes/VOF equations *in* a very small "inner" region of interest, while wave propagation *up to* the "inner" region of interest is solved by existing wave theories. A fully non-linear domain decomposed solver is presented by Paulsen et al. (2014). The fully non-linear potential flow solver is combined with a fully non-linear Navier–Stokes/VOF solver via generalized coupling zones of arbitrary shape.

To generate fully nonlinear boundary conditions for the Navier–Stokes/VOF solver, the potential flow solver "OceanWave3D" developed by Engsig-Karup et al. (2009) is applied. The model solves the three dimensional (3D) Laplace problem in Cartesian coordinates while satisfying the dynamic and kinematic boundary conditions. The equations evolve in time using a classic fourth order, five step Runge–Kutta method. The Laplace equation is solved in a σ-transformed domain using higher order finite differences for numerical efficiency and accuracy. Figure 13.9 depicts a comparison between the irregular wave elevation signal from the OceanWave3D solver, and the same signal measured in the WiFi project for a piston type wave maker.

The Navier–Stokes/VOF governing equations are solved using an open-source computational fluid dynamics toolbox, OpenFoam®. The equations are discretized using a finite volume approximation with a collocated variable arrangement on generally unstructured grids. For the current investigation, OpenFoam® version 2.3.0 is combined with the open-source wave generation toolbox, waves2Foam.

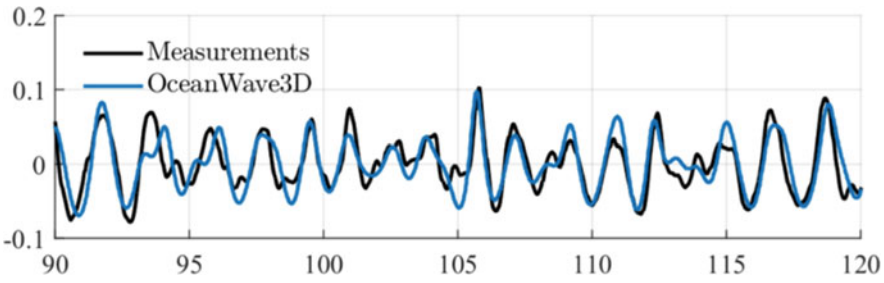

Fig. 13.9 Comparison of irregular wave elevation, experiment vs. OcenWave3D

13.6 Results

13.6.1 Stokes 5th Order

Experimental analyses were conducted within the framework of the AQUILO project on four types of support structures: monopile, gravity based, tripod with pile foundation, and gravity tripod structure (Fig. 13.10). Predictions of wave loads are realized with theoretical JONSWAP energy spectra for a potential 50-year storm condition in the Baltic Sea. Global forces and moments on the structures were measured. The geometries do not represent any existing structures, and were designed for purposes of the AQUILO project, by taking into account typical shapes of existing structures and also the feasibility of manufacturing the physical models.

Due to limitations of the wave maker operability, the depth of the towing tank does not correspond to the design water depths (in a full scale case, the design water depth for a tripod structure is 60 m, while in CTO facilities, the minimum achievable water depth was 120 m). The location of the model relative to the free surface is then adjusted by using an additional support structure mounted to the bottom of the towing tank (Fig. 13.11). Obviously, the difference in water depth results in an incorrect modelling of the wave kinematics. The proposed method of model tests is a necessary compromise resulting from the limitations of the testing facility. In order to minimize the vertical motion of water particles in the vicinity of the foundations, a circular flat plate was mounted below the model (Fig. 13.11).

As a part of this study, experimental results on tripod gravity structure were compared with results from the Morison equation and numerical computations. Waves which excite the structure with the maximum inline force were taken into the

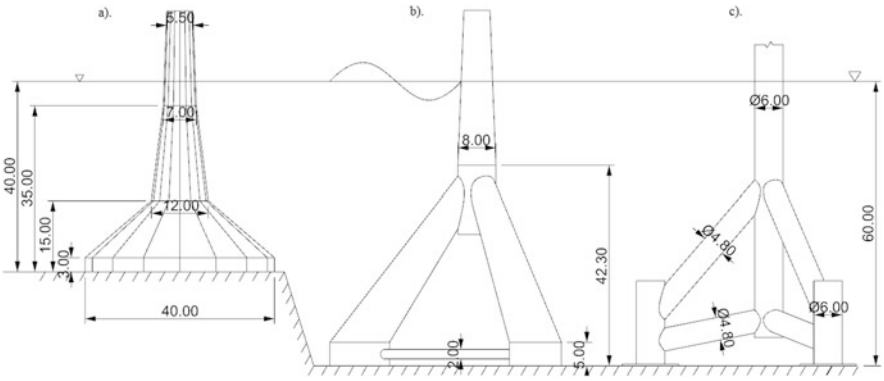

Fig. 13.10 Types of support structures analyzed in the AQUILO project

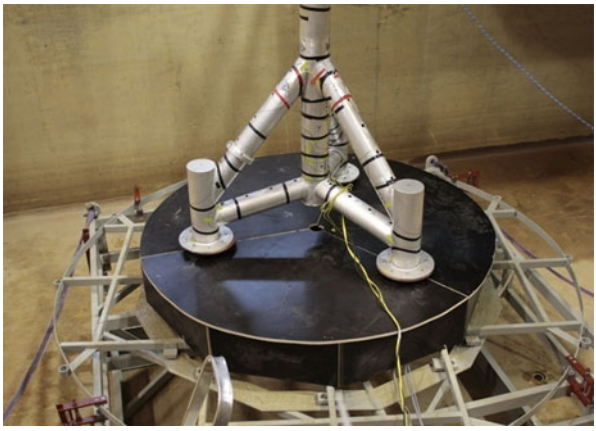

Fig. 13.11 Installation in the towing tank

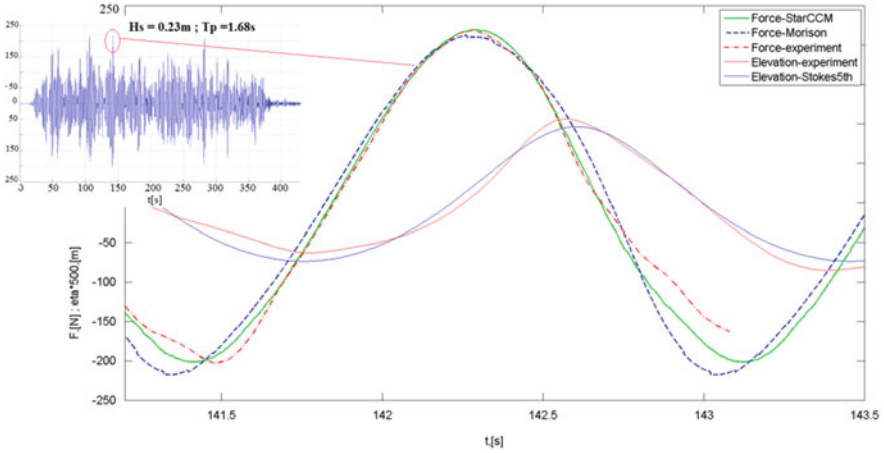

Fig. 13.12 Comparison of inline force; experiment; Morison; Star CCM++

consideration. Drag and inertia coefficients were estimated as Cd = 1.8 and Cm = 2, respectively. The numerical analysis was done with StarCCM++ code, by using the "forcing" technique and an inviscid model. The inviscid model is found to be suitable when the separation of the flow is not expected—i.e.—when the Keulegan-Carpenter number is low (KC < 5) (Faltinsen et al. 1995). A good agreement was observed, as shown in Fig. 13.12.

A local wave breaking was observed during the experimental analysis on the monopile structure equipped with an ice breaking cone (Fig. 13.13). The results of the numerical computation done by StarCCM++ are compared with experimental

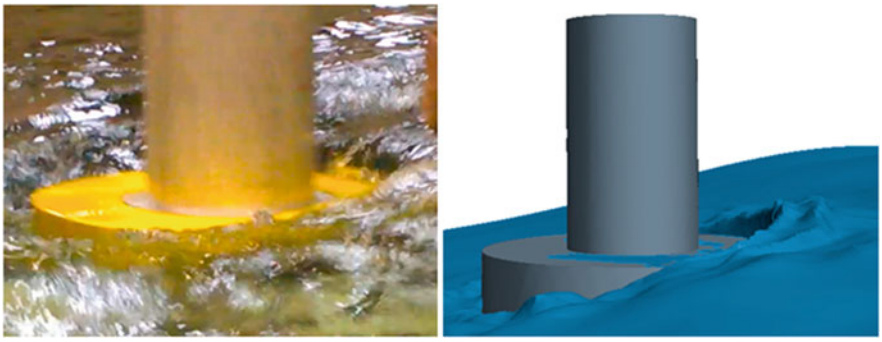

Fig. 13.13 Monopilestructure equipped with ice-breaking cone; experiment vs Star CCM++

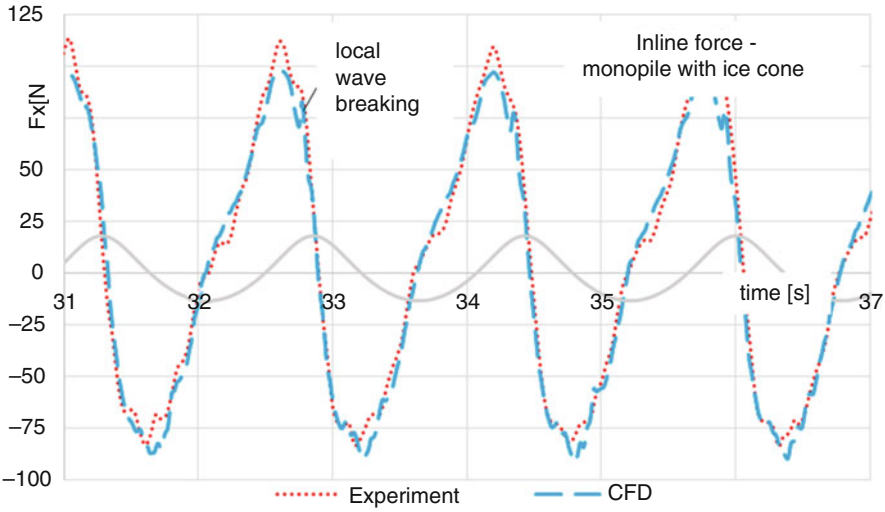

Fig. 13.14 Inline force on monopile equipped with the ice breaking cone; comparison experiment-Star CCM++

measurements for the most violent regular wave which can be simulated in the CTO facilities. The comparison results are shown in Fig. 13.14. Because of experimental limitations, the maximum expected wave height could not be simulated (Hmax ≈ 1.86Hs); thus, another numerical simulation was computed on the maximum expected wave height (Fig. 13.15). An impulse peak force caused by the local breaking of wave on the ice breaking cone is clearly visible: the total force increased by approximately 30 % due to the breaking wave.

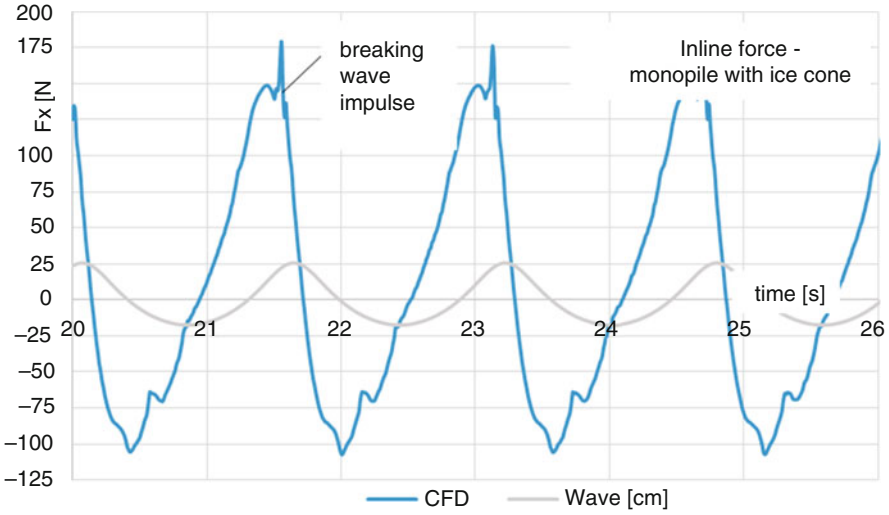

Fig. 13.15 Inline force on monopile equipped with the ice breaking cone; Star CCM++

13.6.2 Breaking Wave

Experimental analyses were conducted within the frame work of the WiFi project on a rigid monopole excited by irregular waves; the waves were estimated using the theoretical JONSWAP energy spectra for an expected 50-year storm condition. A series of impulse forces from breaking waves were observed. The total forces and pressures were measured. Numerical analyses were also conducted by OceanWave3D-OpenFoam interaction, and a good agreement between the measurements and computations was observed (Fig. 13.16).

The examined waves start breaking just before the front of structure, as shown in Fig. 13.17a, b. The pressure field presented in Fig. 13.17c is relative to the stagnation pressure—which is water density ($\rho = 1000$ kg/m^3) multiplied by the squared wave celerity ($c = 2.2$ m/s). The maximum computed pressure peak is $1.5\rho c^2$. The maximum line force (f_i) is calculated as an integration of the pressure field around the circumference of the cylinder (around 40°) and corresponds to the slamming coefficient value $Cs = 1.8$. The values of maximum local pressure and slamming coefficient are lower than any values shown in Table 13.1.

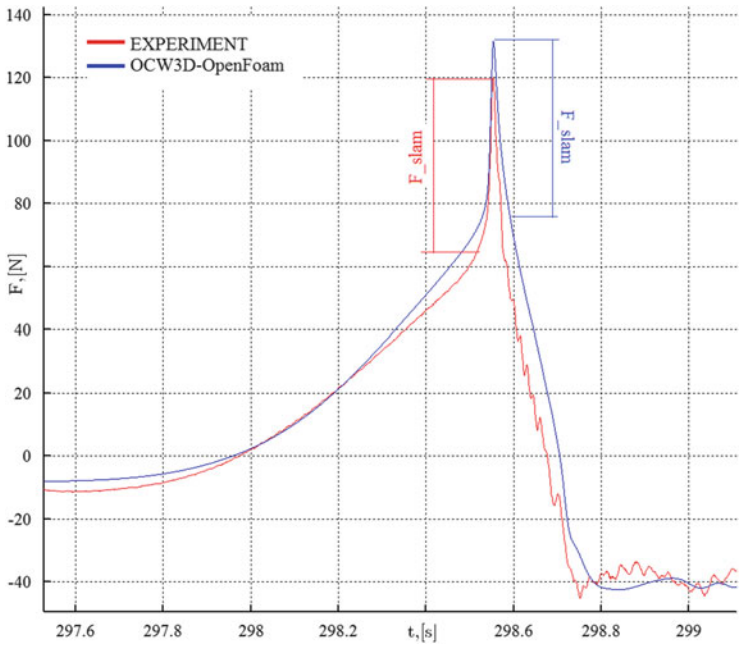

Fig. 13.16 Comparison of inline force; experiments-OceanWave3D & OpenFoam

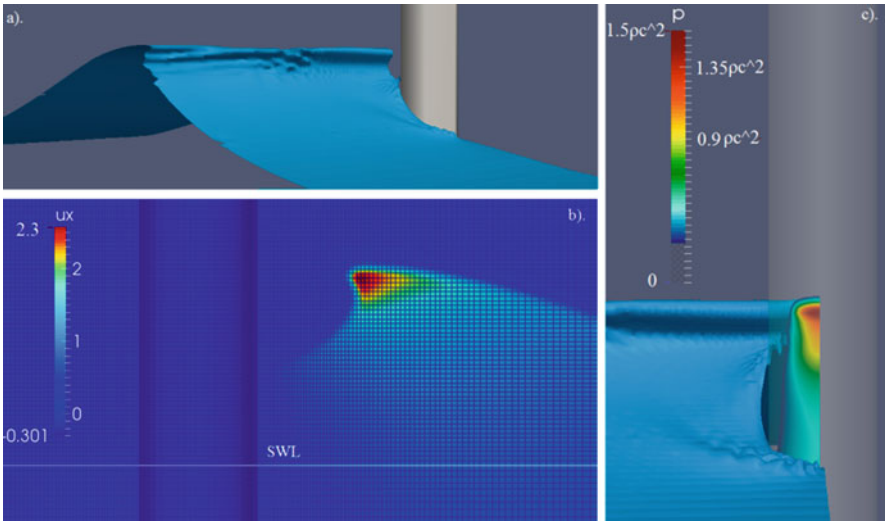

Fig. 13.17 Results from numerical analysis; OceanWave3D&OpenFoam

13.7 Conclusions

A series of computations for hydrodynamic forces on fixed bottom support structures for offshore wind turbines have been carried out. It can be conclusively stated that the Morison equation is an adequate and fast engineering tool for the estimation of inline forces on the slender structures installed in relatively deep water, where strongly non-linear waves are not expected. CFD tools are important for studies related to local flow around the structure, wave run-ups, higher harmonic forces, and impact forces from waves.

It is also noted that simulations of wave propagation (analyses with StarCCM++) suffer from artificial numerical diffusion, especially when k-ε turbulence models are included in the computations. CFD simulations are too expensive and diffusive for simulation of undisturbed wave propagation—which can instead be computed with the potential wave tools, such as OceanWave3D.

An OpenFoam-OceanWave3D interaction was used to simulate breaking waves on a monopile support structure. A very good agreement between measurements and computations was obtained. The maximum obtained peak pressure was $1.5\rho c^2$ and the maximum slamming coefficient (Cs) was 1.8, which is quite low compared to the results of studies presented in Table 13.1.

Acknowledgments The presented work was realized within the framework of AQUILO project (PBS1/A6/8/2012), co-funded by The National Centre for Research and Development and MareWint project under research area FP7-PEOPLE-2012-ITN Marie-Curie Action : "Initial Training Networks". Secondment in Deltares was realized under the framework of the joint industry project WiFi (Wave Impacts on Fixed Turbies).

References

Berberović E, van Hinsberg N, Jakirlić S, Roisman I, Tropea C (2009) Drop impact onto a liquid layer of finite thickness: dynamics of the cavity evolution. Phys Rev E 79(3)

Chan ES, Cheong HF, Tan BC (1995) Laboratory study of plunging wave impacts on vertical cylinders. Coast Eng 25:87–107. doi:10.1016/0378-3839(94)00042-V

Chaplin JR (1993) Breaking wave forces on a vertical cylinder. HMSO, London

DNV (2014) Design of offshore wind turbine structures. Offshore Standard DNV-OS-J101

Engsig-Karup AP, Bingham HB, Lindberg O (2009) An efficient flexible-order model for 3D nonlinear water waves. J Comput Phys 228:2100–2118

Faltinsen OM (1993) Sea loads on ships and offshore structures. Cambridge University Press, Cambridge

Faltinsen OM, Newman JN, Vinje T (1995) Nonlinear wave loads on a slender vertical cylinder. J Fluid Mech 289:179–198

Goda Y, Haranaka S, Kitahata M (1966) Study of impulsive breaking wave forces on piles. In: Reports and technical notes. Port and Airport Research Institute (PARI). Available via PARI. http://www.pari.go.jp/search-pdf/vol005-no06.pdf. Accessed 10 Apr 2016

Hildebrandt A, Schlurmann T (2012) Breaking wave kinematics, local pressures, and forces on a tripod support structure. In: Lynett P, Smith JM (eds) 33rd conference on coastal engineering 2012, Santander, July 2012

Malenica Š, Molin B (1995) Third-harmonic wave diffraction by a vertical cylinder. J Fluid Mech 302:203–229

Morison JR, Johnson JW, Schaaf SA (1950) The force exerted by surface waves on piles. J Pet Technol 5:149–154

Paulsen BT (2013) Efficient computations of wave loads on offshore structures. Dissertation, Technical University of Denmark

Paulsen BT, Henrik B, Bingam HB (2014) An efficient domain decomposition strategy for wave loads on surface piercing circular cylinders. Coast Eng 86:57–76

Pierson WJ, Moskowitz L (1964) A proposed spectral form for fully developed wind seas based on the similarity theory of S. A. Kitaigorodskii. J Geophys Res 69(24):5181–5190

Rainey RCT (1989) A new equation for calculating wave loads on offshore structures. J Fluid Mech 204:295–324

Ros X (2011) Impact forces on a vertical pile from plunging breaking waves. Dissertation, Norwegian University of Science and Technology

Sawaragi T, Nochino M (1984) Impact forces of nearly breaking waves on a vertical circular cylinder. Coast Eng Jpn 27:249–263

Tanimoto K, Takahashi S, Kaneko T et al (1987) Impulsive breaking wave forces on an inclined pile exerted by random waves. In: Edge BL (ed) 20th international conference on coastal engineering, Taipei, November 1986. Coastal Engineering 1986 Proceedings, vol 20. American Society of Civil Engineers, Reston, p 2282

von Karman TH (1929) The impact on seaplane floats during landing. In: National Advisory Committee for Aeronautics (NACA)—Technical Notes NACA-TN-321. Available via NTRS. http://hdl.handle.net/2060/19930081174. Accessed 10 Apr 2016

Wagner H (1932) Über Stoß- und Gleitvorgänge an der Oberfläche von Flüssigkeiten. Z Angew Math Mech 12(4):193–215

Wienke J, Oumeraci H (2005) Breaking wave impact force on a vertical and inclined slender pile-theoretical and large-scale model investigations. Coast Eng 2(5):435–462

Zhou D, Chan ES, Melville WK (1991) Wave impact pressures on vertical cylinders. Appl Ocean Res 13(5):220–234

Chapter 14
Detection of Damage in Metallic Structures for Offshore Applications

Rohan Soman, Paweł Malinowski, and Wiesław Ostachowicz

Abstract Wind energy is seen as one of the most promising solutions to man's ever increasing demands of a clean source of energy. However, a major drawback of the wind energy is the high initial cost for setting up and maintenance. This makes the energy more expensive than the conventional energy sources like fossil fuels and nuclear and hence it has not been widely accepted. Thus, there is a concerted effort to reduce the cost of energy production. This can be achieved by increasing the lifetime of the wind turbines; reducing maintenance costs and ensuring low downtime of the turbine. The lifetime may be increased by ensuring a more robust design while the maintenance cost and the downtime of the equipment may be lowered through the use of condition monitoring (CM) and structural health monitoring (SHM). SHM allows early detection of damage and allows maintenance planning which becomes more important in the off-shore industry where the cost of unscheduled maintenance are high due to the need of specialized equipment. Also, maintenance planning can allow us to avoid unnecessary downtime, hence increasing the availability of the system. In wind turbine structures, tower damage is the third most common damage in wind turbines. Thus, this work concentrates on SHM of a wind turbine tower. A decision level data fusion based on bi-axial tracking of change in Neutral Axis (NA) position is proposed. A discrete Kalman Filter (KF) is employed for the estimation of the NA in the presence of measurement noise from the strain sensors. The KF allows data fusion from the strain sensors and the yaw mechanism for the accurate estimation of the NA. Any change in the NA position may be used as an indicator for the presence and location of the damage. The ratio of the change in the NA along two perpendicular axes is taken and used for the localization. The study has been carried out on the simulated finite element (FE) model of the wind turbine tower and indicates that bi-axial NA tracking based on data fusion is indeed necessary and at the same time is sensitive to damage. The proposed methodology is then validated on real strain data from the Nordtank NTK 500/41 wind turbine. Based on the results presented, the change in NA is indeed a robust damage indicator insensitive to ambient condition changes, and the applied loads.

R. Soman (✉) • P. Malinowski • W. Ostachowicz
Mechanics of Intelligent Structures Department, Institute of Fluid Flow Machinery, Polish Academy of Sciences, ul. Fiszera 14, 80-231 Gdańsk, Poland
e-mail: rsoman@imp.gda.pl; pawel.malinowski@imp.gda.pl; wieslaw@imp.gda.pl

W. Ostachowicz et al. (eds.), *MARE-WINT*, DOI 10.1007/978-3-319-39095-6_14

14.1 Introduction

The main hindrance for more widespread deployment of the wind turbines is the high initial cost for setting up of wind farms and its subsequent maintenance. These high initial costs make the energy more expensive than the conventional energy sources. The cost of generation being the biggest drawback of wind energy, there is a concerted effort to reduce it. This can be achieved by increasing the life-time of the wind turbines; reducing maintenance costs and ensuring high availability. The lifetime may be increased by ensuring a more robust design while the maintenance cost may be lowered and the high availability ensured through the use of condition monitoring (CM) and structural health monitoring (SHM) (Cho et al. 2010). SHM allows early detection of damage and allows maintenance planning which reduces the cost (Doebling et al. 1998). Furthermore, it can allow us to avoid unnecessary downtime, hence increasing the availability of the system.

The SHM needs to be low cost, and suitable for continuous monitoring. These techniques are based on the concept that, the change in mechanical properties of the structure will be captured by a change in its dynamic characteristics (Adewuyi et al. 2009). The SHM process involves the observation of a system over time using periodically sampled dynamic response measurements from an array of sensors, followed by the extraction of damage-sensitive features from these measurements, and the statistical analysis of these features to determine the current state of the system's health. The SHM process requires use of sensors for data collection, filters for data cleansing, and central data processing units for feature extraction and post processing.

SHM has been a field of active research in the aerospace and offshore industry for several decades and many methods have been proposed and investigated. These methods have been able to detect and locate damage in a laboratory environment under controlled conditions. However when these methods were implemented for field validations or in real structures, the results obtained were not up to the desired level. The discrepancy between the expected and the measured results are mainly attributed to the uncertainty in the measurement environment with respect to noise, temperature and excitation mechanism for the structure. Hence there is a search for an SHM system which is able to detect damage in working conditions, and is robust enough to changes in ambient conditions and excitation. Furthermore, the method should be able to detect small levels of damage.

The lack of a standard method for designing an SHM system which will enable us to perform accurate damage detection is the primary motivation of this research.

14.2 Methodology Overview

The scope of the research is SHM of Tower Structures through the measurement of the strain in the tower subject to in-service loading. The methodology is explained here.

14.2.1 Neutral Axis

The primary function of the tower structure is to support the hub, and the nacelle of the wind turbine. The nacelle and the hub are axial loads which are eccentrically loaded on the tower. This eccentric loading gives rise to axial compressive loads as well as bending loads as shown in Fig. 14.1. The axial compression is uniform over the entire cross section while the bending loads will be tensile at one end and compressive at the other. Furthermore, the tower experiences wind loads which result in bending strains in the tower. The axial strains are given by Eq. (14.1):

$$\varepsilon_{axial} = \frac{F}{EA} \tag{14.1}$$

where, ε_{axial} is the longitudinal strain in bending, F is the net axial force due to the nacelle, hub and other wind turbine components, E is the Young's modulus and A is the area of the cross section. Equation (14.2) gives the bending

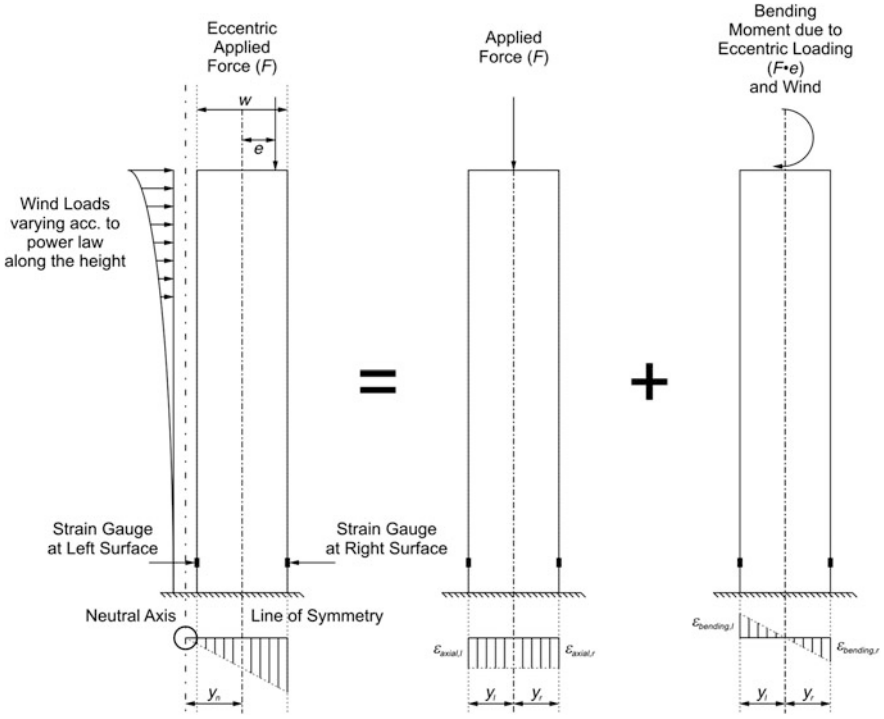

Fig. 14.1 Flexural strain distribution over the cross-section subject to eccentric loading (Soman et al. 2014b)

strains:

$$\varepsilon_{bending} = \frac{M_b y}{EI} \tag{14.2}$$

where, $\varepsilon_{bending}$ is the longitudinal strain in bending, M_b is the net bending moment at the cross section due to wind loading and eccentricity, and I is the area moment of inertia, y is the distance from the NA to the location of the sensor (Xia et al. 2012).

Thus, one surface of the tower experiences, a combination of two axial compressions, (right side, Fig. 14.1) while the other end experiences a combination of compressive load due to the weight and tensile load due to the bending (left side, Fig. 14.1). The net strains on the right and left surface in Fig. 14.1 are given by Eq. (14.3) (Soman et al. 2015b):

$$\varepsilon_{r/l} = -\varepsilon_{axial} \pm \varepsilon_{bending} \tag{14.3}$$

If the line connecting the two strain levels is extended, there will be a point where the strain experienced will be zero, which is identified as the NA point. The NA of the section is a function of the flexural rigidity of the structure, and does not depend on the applied bending loads, thus by, measuring the strains at the opposite edges of the beam, the NA can be located, which in turn may be used as an indicator of the damage. Figure 14.1 explains the abbreviations used and the concept. The NA can thus be estimated based on the strain measurements. This point may be found out by linear extrapolation, and is given by Eq. (14.4) (Soman et al. 2015b):

$$L = \frac{\left(\varepsilon_{bending} - \varepsilon_{axial}\right) \cdot w}{2 \cdot \varepsilon_{bending}} = \frac{\varepsilon_l \cdot w}{\left(\varepsilon_l - \varepsilon_r\right)} \tag{14.4}$$

where, L is the NA Location. It should be noted that the dimensions of the NA location are that of distance, so this metric may be represented as a dimensionless quantity given by Eq. (14.5) (Soman et al. 2015b):

$$NAE = \frac{L}{w} \tag{14.5}$$

The NAE can be made at each time instant based on measured strains at that instance using Eq. (14.5). This approach is termed as direct estimation in further sections, or they can be estimated based on the previous estimates and updated at each time instant using the new measurements using KF which is explained in detail in the later section.

14.2.2 Damage Sensitive Feature

As mentioned, in earlier section, the NA location is independent of the loading conditions, and depends only on the condition of the structure. Thus the % change in the NAE is taken as the damage sensitive feature and is given by Eq. (14.6) (Soman et al. 2015a):

$$\Delta NAE = \frac{NAE_{healthy} - NAE_{monitored}}{NAE_{healthy}} \times 100\% \tag{14.6}$$

The $NAE_{healthy}$ is developed at the time of the installation of sensors when the structure is known to be in healthy condition. $NAE_{monitored}$ is the estimate at every time step. If the % change exceeds a certain threshold, an alarm is raised indicating damage. This threshold is based on sensitivity studies and the tradeoff between the probability of false positive and false negative detections.

14.2.3 Bi-Axial NA tracking

The aim of the SHM system is accurate Level II damage detection. In order to locate the damage, one needs the coordinates of the damage location along the x; y; z axes. The sensor placement at diametrically opposite locations along the tower, as shown in Fig. 14.1, if extended by placing an array of sensors in a line along the tower, can locate the damage along the altitude (z axis). In order to detect the location along the circumference of the tower, we need to perform bi-axial neutral axis tracking. The sensor pairs are placed along mutually perpendicular axes to map the x and y coordinates of damage location. In the polar coordinates, this location can be detected by the angle alone. By the mutually perpendicular sensor placement, the damage can be observed in the form of the sine and the cosine component. The change along x axis is given by the cosine component while along the y axis is given by the sine component of the angle. Thus knowing these components one can determine by taking the tan inverse of the ratio of the changes in the sine and cosine as shown in Eq. (14.7) (Soman et al. 2015b):

$$DL = \tan^{-1}\left(\frac{\Delta NAE_{yaxis}}{\Delta NAE_{xaxis}}\right) \tag{14.7}$$

where DL is the damage location in terms of angle (ϕ).

It should be kept in mind that the periodicity for sine and cosine is 2π while that for tan ratio is π thus leading to loss of directionality. Thus a decision level data fusion is necessary, where the change in the directionality is overcome by proper study of the change in the NA location along both the sensor axes. The sign of the change in the NAE of both the axes determine the exact location of the damage.

14.2.4 Kalman Filter

The KF is a set of mathematical equations that provides an efficient computational (recursive) solution of the least squares method (Welch and Bishop 1995). Theoretically, KF combines a system's dynamic model (physical laws of motion) and measurements (sensor readings) to form an estimate of the systems varying quantities (system state) that is better than the estimate of the system obtained by measurement alone (Welch and Bishop 1995).

The KF allows estimation of the state variable $\boldsymbol{x}$ of a discrete time controlled process governed by the linear stochastic difference equation. In the absence of the control scalar, it can be given by Eq. (14.8) (Brown and Hwang 1997):

$$\boldsymbol{x}_{k+1} = \boldsymbol{A}_k \boldsymbol{x}_k + \boldsymbol{w}_k \tag{14.8}$$

where $\boldsymbol{A}$ is the state transition matrix and $\boldsymbol{w}_k$ is the white process noise, k indicates the time step. The measurement equation is given by Eq. (14.9):

$$z_k = \boldsymbol{H}\boldsymbol{x}_k + \boldsymbol{v}_k \tag{14.9}$$

where $\boldsymbol{H}$ is the measurement matrix that relates to the observation z_k and $\boldsymbol{v}_k$ is the measurement noise.

The goal of using KF is to find an equation that computes a posteriori state $\mathrm{x}_{k/k}$ as a linear combination of an a priori estimate $\boldsymbol{x}_{k/k-1}$ and a weighted difference between an actual measurement z_k and a measurement prediction $\boldsymbol{H}\boldsymbol{x}_{\mathrm{k/k-1}}$ as shown in Eq. (14.10):

$$\boldsymbol{x}_{k/k} = \boldsymbol{x}_{k\ /k-1} + \boldsymbol{K}\left(z_k - \boldsymbol{H}\boldsymbol{x}_{k\ /k-1}\right) \tag{14.10}$$

where $\boldsymbol{K}$ is the Kalman gain. The value of $\boldsymbol{K}$ is chosen to minimise the error covariance. There are several forms of the $\boldsymbol{K}$ matrix discussed in literature. One form of this matrix used for the gain computation is given by Eq. (14.11):

$$\boldsymbol{K}_k = \boldsymbol{P}_{k/k-1}\boldsymbol{H}_k^T \left(\boldsymbol{H}_k \boldsymbol{P}_{k/k-1}\boldsymbol{H}_k^T + \boldsymbol{R}_k\right)^{-1} \tag{14.11}$$

where, $\boldsymbol{P}$ is the error covariance matrix, and $\boldsymbol{R}_k$ is the measurement noise covariance matrix.

Figure 14.2 concisely explains the implementation of the KF in the present application.

The state estimate variable is $\boldsymbol{X}_k = [NAE,\ 1,\ \theta]^T$, NAE in undamaged condition should remain constant independent of the applied loads, the second variable tracked is the constant value 1. This constant is incorporated to ensure, correct relation between the state estimation matrix, the observation matrix and the measurement matrix. The added benefit of the constant is, it makes the measurement matrix square, which allows faster computations. The third component of the vector is the

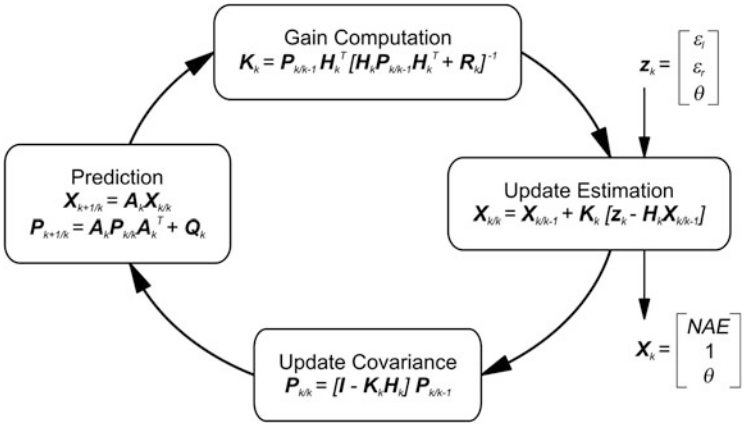

Fig. 14.2 Flow chart for the implementation of the KF (Soman et al. 2014a)

variable θ for the yaw angle. It is a linear estimate of the measurement from the sensor. The input for the KF algorithm is essentially the state transition matrix ($\boldsymbol{A}$), which relates the state estimate variable in time. In this case, $\boldsymbol{A}$ is a unity matrix of dimension 3 as the state estimates are random and not co-related in time. The other input is the measurement matrix ($\boldsymbol{H}$) which links the state estimation variable $\boldsymbol{X}_k$, and the measurement variable ($\boldsymbol{Z_k}$) at each time step (measurement from the sensors).

The H matrix takes into consideration the observability of the NA based on the locations of the sensors and is designed for accurate system modelling while maintaining the linearity of the measurement step. In the present case, $\boldsymbol{Z_k} = [\varepsilon_l, \varepsilon_r, \theta]^T$ vector consisting of the strain measurements from the left (ε_l) and the right side (ε_r) of the tower and the yaw angle measurement (θ) of the nacelle.

14.3 Structure Modelling

The mathematical formulation and the theory discussed in Sect. 14.2 was applied on a FE model of the DTU 10 MW Reference Wind Turbine (RWT) (Bak et al. 2013) for numerical validation. The theory was later validated on the real strain data from the Nordtank NTK 500/41 wind turbine (Paulsen 2011). This section gives the overview of the structures used for the validation and the details of the FE modelling of these structures.

14.3.1 DTU 10 MW RWT

The tower was modelled using the geometric and material properties from the design drawings in commercial FE software ABAQUS. The tower structure was modelled with S4R shell elements. For studying the behavior of the tower to wind loading the dynamic direct analysis was to be carried out. The dynamic analysis uses the modal superposition for estimating the displacements and the strain, so in order to achieve accurate results, and limit the computational load the number of extracted mode shapes was 50. The mesh size of the element was then chosen in order to achieve stable and smooth mode shapes for the extracted modes. The tower was divided in to 82 elements along the height and 48 elements around the circumference. This allowed a reasonable aspect ratio of the shell elements, which lead to a more stable and reliable computation. The tower was encased at the bottom (all DOFs at bottom fixed). The nacelle and hub loads were applied as point loads, at specified eccentricity and height indicated from the design specifications. The wind loads were simulated as random loads using Euro-codes (Standards Norway 2009). A peak wind pressure was selected and applied on the surface area facing the wind, in order to compute the force. The force increases according to the power law along the height of the tower (Sen et al. 2012). The blades, however, were assumed to be pitched into a full aerodynamic brake position to ensure minimal rotor motion and consequent change in mass distribution, which may affect the NA (Bas et al. 2012).

14.3.2 Nordtank NTK 500/41 Wind Turbine

The methodology proposed in Sect. 14.2 was validated from real strain data from the Nordtank wind turbine. The test wind turbine, is located at Risø Campus, Roskilde, and is a traditional Danish three-bladed stall regulated Nordtank (see specifications in Table 14.1).

The wind turbine is instrumented with a variety of sensors on the blades, in the gearbox and on the tower for measuring the different response of the structure and the ambient conditions like strain, the acceleration response to wind loading, the wind speed and direction, the yaw angle, temperature etc. Some of these sensors, namely the strain sensors at the bottom of the tower, the wind speed and direction sensors and the yaw angle measurements have been used for the validation of the methodology. The type of the sensor and its description is given in Table 14.2

Table 14.1 Nordtank NTK 500/41 specifications (Paulsen 2011)

Wind turbine	
8 Risø-R-1593(EN)	
Mechanical brake	High speed shaft, operated in FS-mode
Power regulation	Passive aerodynamic stall
Gearbox	Flender; ratio 1:55.35
Generator	Siemens 500 kW, 4 poles, 690 V
Blade profile	NACA 63-4xx & NACA FF-W3, equipped with vortex generators
Tower type	
Conical steel tube	33.8 m
Hub height	36.0 m
Masses	
Blade weight	1960 kg
Rotor including hub	9030 kg
Tower head mass	24,430 kg
Tower mass	22,500 kg

Table 14.2 Relevant sensor specifications (Paulsen 2011)

Measurement	Sensor	Signal type	Conversion principle	Transmitter
Wind speed nacelle	Risø cup anemometer P2546A with Reed relay	Digital	2 magnets on turning shaft controls the contact closure timings of the relay per revolution	Risø P2858A DAU configured to periodic time measurement
Wind direction nacelle	Vector Wind vane F2819A	Analogue	Measuring on resistive viper path relative to one full turn	Voltage divider
Tower bottom bending moment X	Micro Measurement Strain Gauge CEA-06-250C-350	Analogue	Semiconductor foil subjected to resistive change due to bending	Risø P2912B SG Amplifier
Tower bottom bending moment Y	Micro Measurement Strain Gauge CEA-06-250UW-350	Analogue	Semiconductor foil subjected to resistive change due to bending	Risø P2912B SG Amplifier
Position of nacelle	Resistor with gearbox attached to yaw drive	Analogue	Measuring on resistive path	Voltage divider

14.4 Numerical Simulations

The methodology highlighted in Sect. 14.2 was applied on the numerical models described in Sect. 14.3.1. The goals of the simulations were to:

- Establish the need for KF based NA tracking
- Establish NA as a damage sensitive feature
- Perform Level II damage detection using Bi-Axial NA tracking
- Establish the robustness of KF based NA tracking methodology

14.4.1 Need for KF tracking

The KF as explained in Sect. 14.2.4 combines the previous estimate of the state and the new estimate based on the measurements. Thus in noisy conditions, the KF based estimation is much more stable than the direct estimation. Also, in the second section it was outlined how one can estimate the NA from the instantaneous measured strains. This section compares the NA estimation by these two methods in different simulated conditions. The measured strains and the yaw angle were taken as input to the system and the NA location was estimated by both the methods. The measured signal was contaminated with different levels of white noise in order to simulate real conditions. Table 14.3 shows the statistical performance of the two estimation methods.

As can be seen, the KF needs some initial time for the convergence, but once the convergence is achieved the estimation is more stable. This can be seen from the lower standard deviation in the NA estimate observed while using the KF estimation than that using the direct estimation. Furthermore, it can also be seen that the mean NA position for the KF based estimation is more stable than that using direct estimation. The more stable mean will allow us to set lower thresholds for the change in NA position. This in turn will allow detection of small levels of damage in the tower structure.

Thus, use of KF improves the estimation, and as such, is recommended for accurate NA tracking. Furthermore, the KF algorithm is ideally suited for data

Table 14.3 Statistical performance of estimators (Soman et al. 2015a)

Scenario	KF estimation standard deviation (mean)	Direct estimation standard deviation (mean)
0 % Noise for strain and 0 % noise for yaw angle	0.0444 (1.633)	0.1064 (1.637)
5 % Noise for strain and 0 % noise for yaw angle	0.0474 (1.633)	0.1862 (1.622)
10 % Noise for strain and 0 % noise for yaw angle	0.0507 (1.635)	0.4527 (1.666)
0 % Noise for strain and 5 % noise for yaw angle	0.0444 (1.633)	0.1168 (1.641)
5 % Noise for strain and 5 % noise for yaw angle	0.0499 (1.633)	0.211 (1.686)

fusion, and hence the yaw angle tracking can be seamlessly included in the algorithm in order to increase the confidence level in the NA tracking.

14.4.2 NA as a Damage Sensitive Feature

As explained in the earlier section, the NA of the cross-section of the tower is the property of the condition of the structure and may be used as a damage indicator. In order to validate the use of NA as damage indicator, artificial damage was introduced in one element of the tower, by reducing the flexural rigidity of that particular element by 20 %. The simulated damage was detected by comparing the NAE of the damage and the undamaged element. The relative change in the location of the NA is given in Table 14.4.

The damage is detected if the change in the NA estimation of the damaged and undamaged state is more than a specified threshold, which is determined based on simulated studies of different damage scenarios (Soman et al. 2015a). As can be clearly observed, even in the presence of measurement noise, there is significant difference in the change of the NAE of the damage element and the others, so the

Table 14.4 NA based damage detection in presence of noise (Soman et al. 2014a)

Sensor location (m)	NAE (%)			
	0 % Noise	1 % Noise	5 % Noise	10 % Noise
2.875	−0.0177	−0.0694	−0.2029	0.5403
8.625	−0.1546	−0.1266	−0.3123	0.3565
14.375	−0.0820	−0.0576	−0.1811	0.1504
20.125	−0.2128	−0.2161	−0.3438	−1.0455
25.875	−0.0252	−0.0508	−0.0135	0.5836
31.625	−0.4384	−0.4577	−0.4394	0.7286
37.375	−0.9947	−1.0899	−1.0932	−1.1910
43.125	**5.4836**	**5.4674**	**5.4675**	**5.3286**
48.875	−1.0367	−1.0491	−0.9949	−0.7893
54.625	−0.4416	−0.5153	−0.6243	−0.1339
60.375	−0.0422	0.0151	−0.1978	0.1797
66.125	−0.2413	−0.2820	−0.2334	−0.3370
71.875	−0.1271	−0.0716	0.1087	0.3750
77.625	−0.1664	−0.1475	−0.1069	−0.0487
83.375	−0.0417	−0.0639	−0.0125	−0.2715
89.125	−0.0770	−0.1277	−0.0120	−0.4831
94.875	0.0101	0.0301	0.1279	−0.2785
100.625	−0.0121	−0.0271	−0.3458	0.1291
106.375	0.0584	0.0463	0.0330	0.0299
112.440	−0.0368	0.0684	0.1646	0.7457

chances for a false detection are quite minimal and as such a lower threshold may be possible 1 % in the case where yaw angle is being tracked as well. Thus NA can be used as a robust damage sensitive feature.

14.4.3 Bi-axial NA tracking

NA may be used as a damage sensitive feature. Table 14.2 only gives the location of the damage along the altitude. In order to isolate the damage even further, bi-axial NA tracking is necessary. For bi-axial NA tracking, two mutually perpendicular sensor pairs are necessary as explained in Sect. 14.2.3. Then the change in NA can be mapped along the two axes and the exact location determined. In order to show the methodology, four different damage scenarios were simulated, as shown in Fig. 14.3.

Table 14.5 shows the change in NA along the two axes, and as can be seen through decision level data fusion, we can easily isolate the damage accurately.

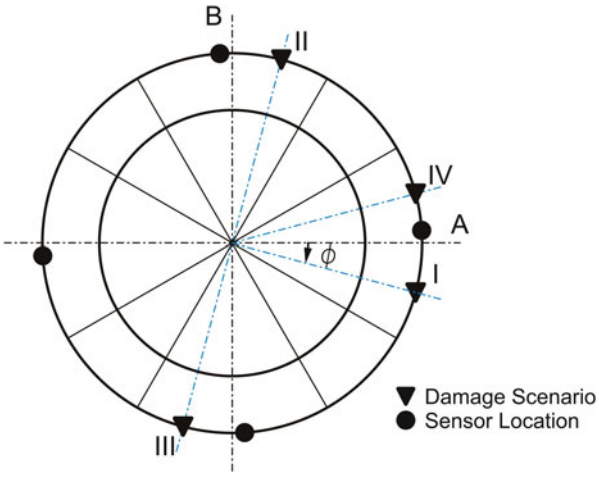

Fig. 14.3 Damage scenarios indicating the need for bi-axial NA tracking (Soman et al. 2015b)

Table 14.5 Bi-axial NA tracking for damage detection (Soman et al. 2015b)

Damage scenario	ΔNAE_A (%)	ΔNAE_B (%)	Damage location (°)	Damage location predicted (°)		Error in detection (°)	
				Fusion	W/o fusion	Fusion	W/o fusion
I	6.264	−2.020	−15	−17.9	−17.9	2.9	2.9
II	2.003	6.206	75	72	72	3	3
III	−2.301	−6.607	−105	−109	**70.7**	4	**−175.7**
IV	12.800	**0.875**	15	**3.8**	**3.8**	**11.2**	**11.2**

The damage scenario I and II indicate the validity of the decision level data fusion, and taking the ratio of the changes in NA, is a valid technique for fusion. The damage isolation for case I and II is valid without fusion as the damage lies in the $-90°$ to $90°$ range. Damage scenario III is a point diametrically opposite to II and it shows the significance of decision level data fusion. If the signs corresponding to the change of the location are not taken into account the isolation give a diametrically opposite point which may be termed as false isolation of the damage (shown in bold values in Table 14.5) and hence the decision level data fusion is necessary. Damage scenario IV indicates that when the damage is at locations perpendicular to one of the axes, the results obtained for the isolation are not accurate, but this in essence proves that bi-axial tracking is indeed necessary.

It can be noted that the change in the location of NA in scenario IV, in the estimate at A, is significant and hence false detection of the damage is highly unlikely. The high change exceeding 10 % also indicates very close proximity of the damage to the strain sensors and gives further idea about the location of the damage. Furthermore, the decision level data fusion will recognize that the threshold for the damage detection has not been exceeded (shown in bold values in Table 14.5) and as such the data should not be used, thus making the decision level data fusion based strategy more robust against false localization.

14.4.4 Robustness of KF

The ideal SHM methodology should need limited operator skill and should be objective in nature. The previous section formally introduced a methodology for the selection of the threshold for damage detection which allows the methodology to be objective. In order to make it independent of operator skill the methodology should be robust in nature. This section shows how the KF is a robust methodology requiring limited operator skill for setting up. The Kalman Filter is a powerful tool for the estimation of the state variables especially in the presence of measurement noise. The NA estimate is independent of the initial setting up of the NA, and as such this makes the damage detection methodology robust. Figure 14.4 shows the evolution of the prediction under different parameters of the KF initiation.

Figure 14.4a shows the estimate of NA for different initial guess locations of the NA. As can be seen NA estimate is independent of the starting position, and converges to the true value in relatively short time and as such the damage detection methodology is not affected. Figure 14.4b shows the independence of the initial NA estimate to the uncertainty of the initial guess location or in other words the covariance of the state matrix. The value affects the rate at which the convergence is achieved.

As can be seen lower the value of the covariance quicker the convergence is achieved. Figure 14.4 shows the effect of the uncertainty in the strain measurements on the NA estimate. This uncertainty is termed as measurement noise.

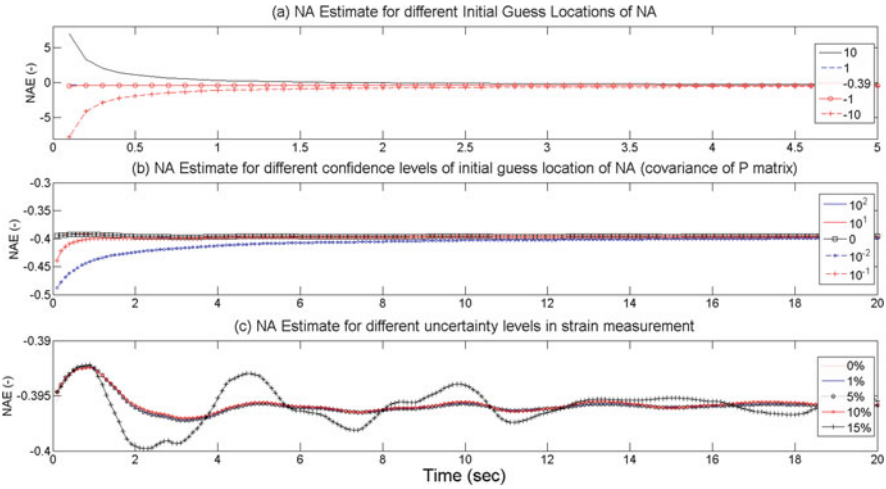

Fig. 14.4 Sensitivity of NAE to KF parameters (Soman et al. 2015a)

It is intuitive to think that greater the measurement noise, more unsteady is the NA estimate, which in turn affects the threshold value for damage detection. It can be seen that even at 10 % measurement noise, the KF estimate is more or less stable, which points towards the robustness of the KF based methodology.

14.5 Validation

The success of the methodology for damage detection was checked on simulated damage scenarios. But the methodology needs to be validated with application on real structure. This chapter thus aims at validating the methodology with available strain data from the NTK 500/41 Wind Turbine.

The sensors were placed on the wind turbine as explained in Sect. 14.3, and are capable of measuring only the bending moments. Also, it is not feasible to introduce any damage in the structure, as the structure is in-service. Also the insurance for the machine will be void if such changes are made to the system. Hence, the study is limited to validating the need for KF based NA tracking. The results are shown and discussed in detail in the subsequent sections.

14.5.1 Need for KF Based NA Tracking

As explained earlier the direct estimation method for the NA tracking estimates the NA position based on the instantaneous strain measured by the system. In

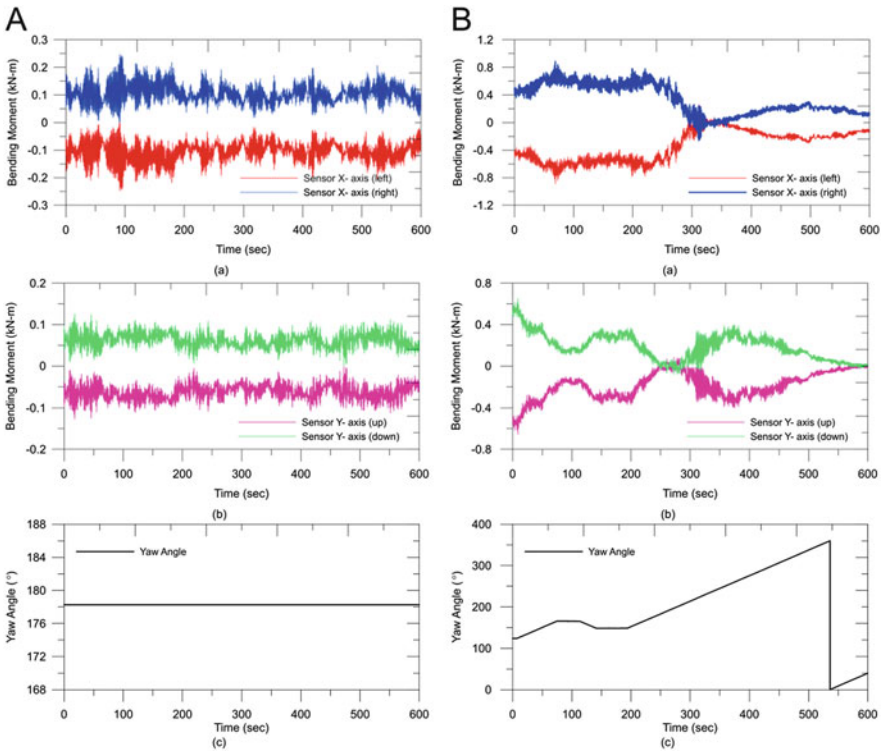

Fig. 14.5 Measurements from Nordtank NTK 500/41 wind turbine. (**A**) Fixed yaw angle condition, (**B**) changing yaw angle condition. (a) Bending moment along x-axis, (b) bending moment along y-axis, (c) yaw angle measurement

the presence of measurement noise, this may lead to inaccurate NA estimation. On the other hand KF makes use of some component of the earlier estimate and then incorporates the new measurements of strain, in order to yield a more stable estimation.

In order to ascertain the performance of the two methods, the strain and yaw angle measurements from the Nordtank NTK 500/41 wind turbine were used for the NA estimation. Figure 14.5A(a) and (b) show the strains measured when the yaw angle was more or less constant (Fig. 14.5A(c)). Figure 14.5B(a) and (b) show strain measurements for the condition when the yaw angle was changed constantly (Fig. 14.5B(c)).

Based on these inputs the NA was tracked using the two methods. Figure 14.6 shows the performance of the direct estimation and KF estimation methods for the fixed yaw angle condition and Fig. 14.7 shows the performance in changing yaw angle conditions. The NA estimation is more stable in both the methods for fixed yaw angle conditions as the mass distribution is constant and the bending strains are more or less constant. Also, it can be clearly seen the NAE is more stable using

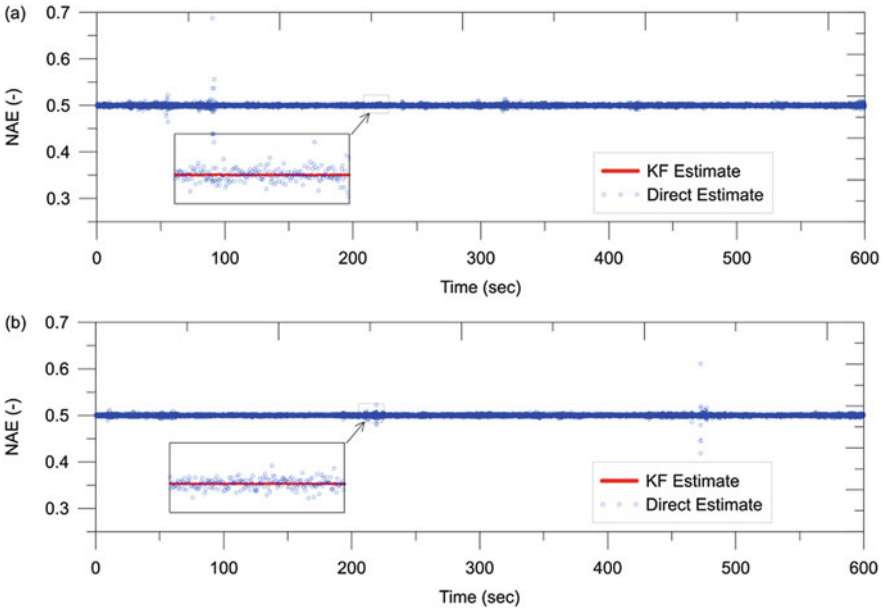

Fig. 14.6 Comparative performance for NA estimation for fixed yaw angle condition (**a**) along x-axis (**b**) along y-axis (Soman et al. 2015c)

the KF estimate. The direct method gives erroneous estimation especially when the strain values are close to 0. This is in keeping with intuition, as when the measured strain is low, the effect of sensor noise and localized changes becomes significant leading to false estimations.

Figure 14.8 gives the comparative performance of the two methods under both the working conditions. It can be clearly observed that the standard deviation of the KF based estimation method is orders of magnitude better than the direct estimation method. Also, the mean of the KF based estimate is more accurate than the direct method.

The more accuracy in the estimation allows us, in turn, to have stricter thresholds for the damage detection. The lower thresholds allow earlier damage detection. Also, in the case of direct estimation, where the standard deviation of the estimate is higher, there is a higher possibility of a false negative damage detection, which leads to higher downtime and lower availability.

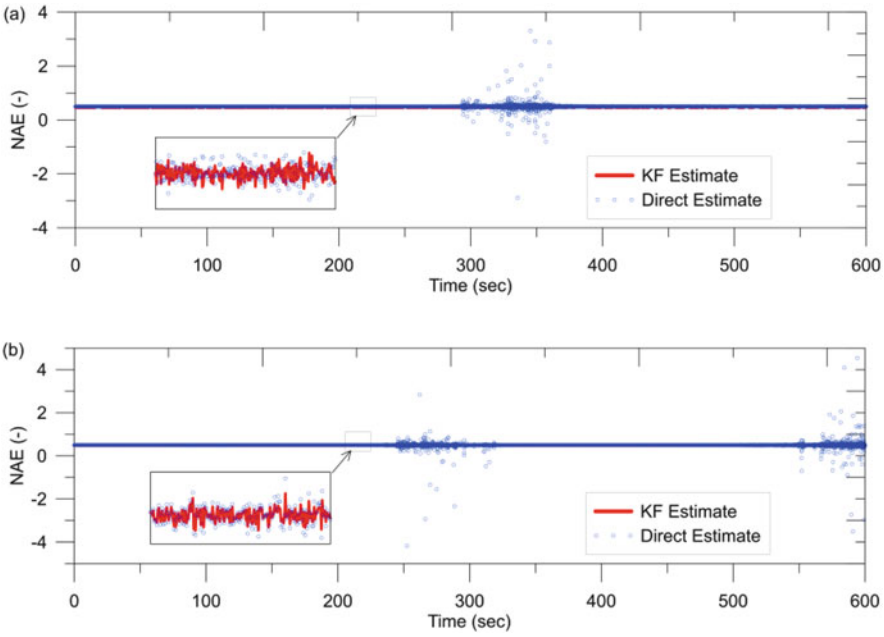

Fig. 14.7 Comparative performance for NA estimation for changing yaw angle condition (**a**) along x-axis (**b**) along y-axis (Soman et al. 2015c)

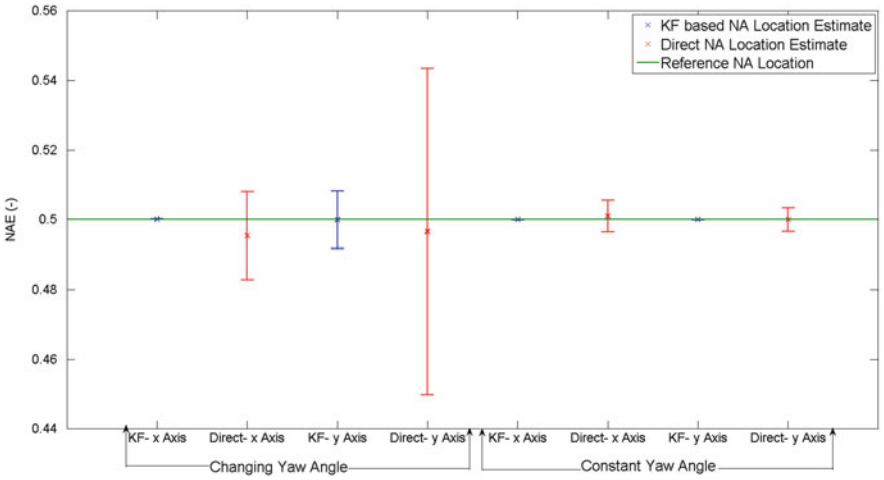

Fig. 14.8 Statistical performance comparison for NA estimation (Soman et al. 2015c)

14.6 Conclusions

The present research presents a complete damage detection methodology for tower structures of offshore wind turbine structures. The methodology makes use of NA as a damage sensitive feature. The NA as a damage sensitive feature has been proposed in literature for bridges (Sigurdardottir and Glisic 2013, 2014), but the innovation of the research is the customization of the NA tracking to the wind energy applications. The method makes use of KF for accurate NA tracking. The KF is robust tool ideally suited for data fusion and allows us to seamlessly combine the yaw angle measurement in the NA estimation and in turn improve the confidence level of the NA estimate. The KF uses the instantaneous strain measurements and a part of the previous estimate of NA location to give a more stable estimate than the one given by the direct method. The KF based estimations are shown to be more precise and accurate as compared to the estimation by the direct estimation. This has been shown through several simulated studies under different conditions of measurement noise as well as through actual strain measurements.

The NA seems to be a robust indicator and is not affected by the ambient loads as well as temperature conditions. Also, through the use of decision level data fusion, one can easily isolate the damage. The method also highlights a method to determine the threshold for the damage detection alarm to be raised. The threshold is chosen based on the trade-off of false detections and this threshold has been successfully implemented on the data from the Nordtank NTK500/41 wind turbine.

In the present study only the bulk temperature effects have been considered, and any temperature gradient effects are expected to be negligible because of the metallic construction and relatively thin cross section. Lastly the blades have been considered to be in braked condition in order to avoid any rotation and the resultant change in mass of the system. It is envisaged that the rotation effects can be easily incorporated through the data fusion of the rotation speed and a wavelet based filtering of the strain cycles due to the rotation. In addition, the present damage detection studies have been limited to reduction in the flexural rigidity of one element of the tower. Although this approach is commonly used in SHM of structures, is not a realistic damage scenario. Thus the performance of the NA tracking methodology must be validated for the detection of some realistic damage scenarios like fatigue cracks, or loosening of the bolts at the connecting flange. These are two areas identified for the future work, along with validation on strain data from a damaged tower structure.

Acknowledgments The authors would like to acknowledge the European Commission for their research grant under the project FP7-PEOPLE-20120ITN 309395 “MARE-WINT” (new Materials and REliability in offshore WINd Turbines technology). The authors would also like to thank DTU Wind Energy, for providing valuable information for the modeling of the 10 MW RWT tower for the purpose of this study. The authors are also grateful to TASK-CI for allowing the use of their computational resources. The opinions expressed in this paper do not necessarily reflect those of the sponsors.

References

Adewuyi A, Wu Z, Serker N (2009) Assessment of vibration-based damage identification methods using displacement and distributed strain measurement. Struct Health Monit 8(6):443–461

Bak C, Zahle F, Bitsche R et al (2013) The DTU 10-MW reference wind turbine. In: DTU orbit—the research information system. Available via Technical University of Denmark. http://orbit.dtu.dk/files/55645274/The_DTU_10MW_Reference_Turbine_Christian_Bak.pdf. Accessed 06 Apr 2016

Bas J, Carriveau R, Cheng S et al (2012) Strain response of a wind turbine tower as a function of nacelle orientation. In: Dini P, Lorenz P (eds) Proceedings of BIONATURE 2012: the 3rd international conference on bioenvironment, biodiversity and renewable energies, St Maarten, 2012

Brown R, Hwang P (1997) Introduction to random signals and applied Kalman filtering. Wiley, New York

Cho S et al (2010) Structural health monitoring of cable-stayed bridge using acceleration data via wireless smart sensor network. In: Frangopol DM, Sause R, Kusko CS (eds) Bridge maintenance, safety, management and life-cycle optimization: proceedings of the 5th international conference on bridge maintenance, safety and management, Philadelphia, July 2010. CRC Press, London, p 85

Doebling S, Farrar C, Prime M (1998) A summary review of vibration based damage identification techniques. Shock Vib Dig 30(2):91–105

Paulsen U (2011) Verification of long-term load measurement technique: work package 1B.2 under the European Commission, integrated wind turbine design (UPWIND). In: DTU orbit—the research information system. Available via Technical University of Denmark. http://orbit.dtu.dk/files/5712228/ris-r-1782.pdf. Accessed 10 Apr 2016

Sen Z, Altunkaynak A, Erdik T (2012) Wind velocity vertical extrapolation by extended power law. Adv Meteorol. doi:10.1155/2012/178623

Sigurdardottir D, Glisic B (2013) Neutral axis as damage sensitive feature. Smart Mater Struct. doi:10.1088/0964-1726/22/7/075030

Sigurdardottir D, Glisic B (2014) Detecting minute damage in beam-like structures using the neutral axis location. Smart Mater Struct. doi:10.1088/0964-1726/23/12/125042

Soman R, Malinowski P, Ostachowicz W (2014a) Neutral Axis Tracking for damage detection in wind turbine towers. Paper presented at the European Wind Energy Conference and Exhibition (EWEA), Barcelona, 10–13 March 2014

Soman R, Malinowski P, Ostachowicz W (2014b) Kalman Filter based data fusion for neutral axis tracking for damage detection in wind-turbine towers. In: Abstracts of the 7th European workshop on structural health monitoring, EWSHM, Nantes, 8–11 July 2014

Soman R, Malinowski P, Ostachowicz W (2015a) Threshold determination for neutral axis tracking based damage detection in wind turbine towers. Poster presented at the Offshore 2015. European Wind Energy Association, Copenhagen, 10–12 March 2015

Soman R, Malinowski P, Ostachowicz W (2015b) Bi-axial neutral axis tracking for damage detection in wind-turbine towers. Wind Energy 9(4):639–650

Soman R, Malinowski P, Ostachowicz W et al (2015c) Kalman filter based data fusion for neutral axis tracking in wind turbine towers. In: Kundu T (ed) Proceedings of the SPIE 9438, health monitoring of structural and biological systems, California, 2015

Standards Norway (2009) Eurocode 1: actions on structures—part 1–4: general actions—wind actions. NS-EN 1991-1-4:2005+NA:2009, Lysaker

Welch G, Bishop G (1995) An introduction to the Kalman filter. In: Technical reports, Department of Computer Science University of North Carolina at Chapel Hill. Available via UNC CS. https://www.cs.unc.edu/~welch/media/pdf/kalman_intro.pdf. Accessed 10 Apr 2016

Xia H, Ni Y, Ye X (2012) Neutral-axis position based damage detection of bridge deck using strain measurement: formulation of a Kalman filter estimator. Paper presented at the 6th European workshop on structural health monitoring, Dresden, 3–6 July 2012

Part IV
Reliability & Preventive Maintenance of Offshore Wind Turbines